Radiomics in Medical Imaging with Application to Surgical Innovation

Prabhakara Subramanya Jois

A Thesis

in

The Department

of

Computer Science and Software Engineering

Presented in Partial Fulfillment of the Requirements

for the Degree of

Master of Applied Science (Software Engineering) at

Concordia University

Montréal, Québec, Canada

April 2022

Abstract

Radiomics in Medical Imaging with Application to Surgical Innovation

Prabhakara Subramanya Jois

Modern surgery today has greatly improved healthcare due to technological advancements in medical imaging. It has fostered a culture of innovation that has progressed with continuous and incremental changes towards curing patients' ailments. With evidence-based assessments gaining prominence in modern surgery, Radiomics has become crucial to resolving problems through the integration of the best scientific data with the correct clinical expertise. As a quantitative approach to medical imaging, Radiomics uses mathematical analysis to improve the data made available to clinicians, which greatly influences their decision-making ability. In this thesis, we focus on two applications: pelvic bone segmentation from CT data for designing patient-specific customizable pessaries; and quantitative assessment of breast morphology, for reconstructive breast surgeries.

For pelvic bone segmentation, we investigate several encoder-decoder network configurations trained on limited data and use histogram based features from Radiomics to take a data-centric view towards the problem and boost the model performance on completely unseen data through histogram specification. Then we evaluate the performance on two publicly available CT datasets.

For assessment of breast morphology, we propose a novel metric for quantifying the overall dissimilarity between two breast mounds, called VIMA, by using shape and size based features from iso-contours. The methodology was experimented on 3D scans of artificial breasts and found to be highly useful in an intra-operative setting for aiding surgeons during aesthetic breast surgeries.

आचार्यात् पादमादत्ते पादं शिष्य स्वमेधया |
पादं सब्रह्मचारिभ्य: पादं काल क्रमेण च ||

One part from the teacher, One part from self-study,
One part from colleagues, And one part from the passage of time.

Acknowledgments

First and foremost, I would like to convey my deepest gratitude towards my supervisor Dr. Thomas Fevens for his guidance and countless contributions towards my all-round development during the course of my Master's. I particularly appreciate his wise and humorous counsel which extended beyond academia and touched on all matters of life. I have been very fortunate to have an understanding advisor like him, who's supported me throughout my academic and entrepreneurial journey.

Secondly, I would like to extend my gratitude for the comradery by members of ML-MVP Lab, colleagues at my startup - OpAI Innovations, and teammates from FemTherapeutics. Special thanks to my band of brothers - S. Suresh, S. Srinath, R. Adhikari, R. Ramesh and T. M. Prajwal, for being present during the dark times of COVID-19.

Next, I would like to thank the Surgical Innovation program, the cross-disciplinary graduate program from Concordia, McGill and ETS, as it provided me with a unique opportunity to understand the art of finding opportunities. It also provided the necessary financial support for my stay in Montreál. Lastly, I want to thank my parents for their selfless love and continuous encouragement.

I dedicate this dissertation to my parents and my future partner.

Contents

List of Figures

List of Tables

Chapter 1

Introduction

In this chapter, we provide a brief introduction to this thesis, while describing our usage of Radiomic features with application to Surgical Innovation, and our Contributions to the target applications. Then we provide an outline of this thesis.

1.1   Surgical Innovation

Today, due to the advancements in healthcare technologies, *modern surgery* has greatly improved healthcare for patients while fostering a culture of innovation. Here, patients seek the latest methodologies for obtaining desirable outcomes [1]. Such consistent innovation in the field of medical imaging and digital-health has led to the evolution of evidence based-medicine (EBM). Since, the field of medicine has had a long history of using objective approaches for the scientific inquiry of diagnosis and treatment of ailments [2], EBM was introduced as a descriptive method of educating medical practice for enhancing a physician's decision making ability. The EBM method naturally evolved to prioritize objective assessment of any clinical observations, for producing evidence of clinical effectiveness. Such evidence had to be shown explicitly, based on systemic guidelines and questioners that tried to quantify any clinical analysis. In this context, *Radiomics* became crucial for resolving clinical problems, through the integration of best scientific data with the appropriate clinical expertise [3].

Histogram based features		Shape and Size based features	Texture features	
Whole pixel value	Positive pixel value		Based on ISZ	Based on GLCM

3D geometric properties of the tumor

Size of each area with pixels of the same intensity level

Spatial distribution of voxel intensities in thirteen directions

— Whole pixel
— ROI outer 1/3
— ROI inner 2/3
— ROI delta

ROI outer 1/3

ROI delta

ROI inner 2/3

Quantifying tumor intensity characteristics using first-order statistics, calculated from the histogram of tumor voxel intensity values

ISZ, Intensity variance and size zone variance value; GLCM, Gray-level co-occurrence matrix; ROI, Region of interest

Figure 1.1: Illustration of Radiomics based quantitative features for tumor assessment from computed tomography imaging [5].

As a quantitative approach to medical imaging, *Radiomics* uses mathematical analysis to improve the data made available to clinicians [4, 5]. Here, handcrafted features are extracted through the image pixel interrelationships, and spatial distribution of their intensities, to perform image analysis better, as seen in Fig. 1.1. Radiomics is also used to extract information from clinical data by employing analysis methods from Deep learning [6]. So far numerous works of research from various domains of imaging have demonstrated the potential of Radiomics to improve diagnostic and prognostic decision making in a clinical setting [7]. But a major challenge is present, due to a gap between what is known and what is needed in the clinic, which produces results lacking in clinical utility. In our work, We try to bridge that gap for two target applications.

2

1.2 Contribution of this Thesis

In this thesis, we focus on the following applications, (a) pelvic bone segmentation from computed tomography (CT) data for designing patient specific customizable pessaries, (b) quantitative assessment of breast morphology from 3D data, for reconstructive breast surgeries.

For pelvic bone segmentation, we introduce an encoder-decoder network trained on limited data, with an augmented BCE-IoU loss. Then using histogram based radiomic features, we take a data-centric view towards the problem and boost the model performance on completely unseen data through histogram specification. And evaluate the performance on two publicly available CT-datasets.

For assessment of breast morphology we propose a novel metric, VIMA, using shape and size based radiomic features from iso-contours, for quantifying the overall dissimilarity between two breast mounds. The methodology was experimented on 3D scans of artificial breasts, and based on feedback from three plastic surgeons VIMA was found to be highly useful in an intra-operative setting for aiding surgeons in reducing incidence of breast asymmetry.

1.3 Outline of this Thesis

The remainder of the thesis is organized as follows: In Chapter 2 we provide background information on some traditional and deep learning based techniques, employed in our target applications. In Chapter 3, we present our pelvic bone segmentation work on CT-data along with its experimental results. In Chapter 4, we present our novel methodology, VIMA, for assessing breast asymmetry and provide measure of system usability. In Chapter 5, we conclude this thesis and discuss some future work and research directions.

Chapter 2

Background

In this chapter, we will briefly cover the background information related to Medical image assessment, for improving clinical utility through radiomic features in our target applications: (a) pelvic bone segmentation from CT data for designing patient-specific customizable pessaries, (b) quantitative assessment of breast morphology, for reconstructive breast surgeries.

2.1 Medical Image Analysis

It is the practice of analysing an image of a body for clinical examination and medical intervention, as well as a visual depiction of particular organs or tissues [8, 9]. This practice aims to expose hidden interior structures beneath the skin and bones, as shown in Fig. 2.1, allowing for anomalies to be detected. And for the target applications in our work, we utilize medical data obtained from CT scans and three Dimensional (3D) scans.

CT-Scan

A CT scan is an imaging technique where a scanner with rotating X-ray tubes transmits rays across the body. Here, the detectors within the scanner measure the ray's attenuation through the different layers within the body, which allows for the detection of tissues with varying densities. Such measurements taken from multiple viewpoints are processed to produce a cross-sectional image. A sufficiently resolved CT image can provide detailed information on various structures like
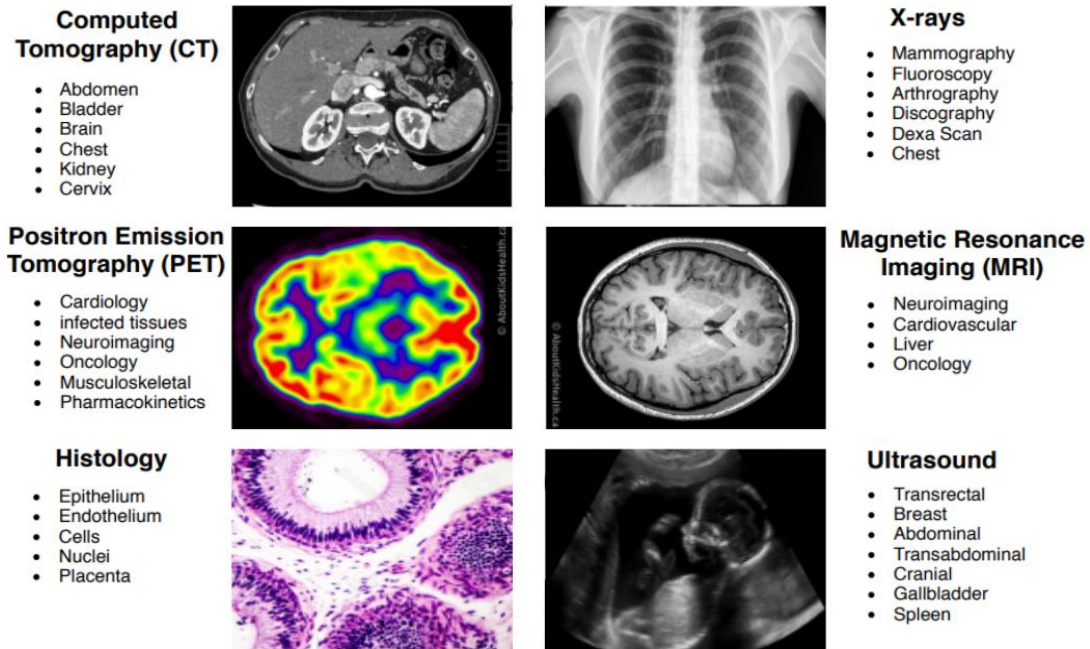
Figure 2.1: Illustration of different medical imaging modalities (modified from [9]).

vasculature, organs, bones and their surrounding tissue [10], along with other parts that are useful for the detection and diagnosis of ailments.

3D Scanning

Three Dimensional scans are commonly used to produce three-dimensional data of any free-form objects by generating their point clouds or triangular meshes. The 3D data is formatted into a standard reference system, often merged with proper alignment to form a complete model. A common 3D scanning technique involves a structured light [11] where a projector casts a sequence of light patterns on the target object, and a camera captures an image of the deformed light pattern, which is used to compute the depth information. Methods like time-of-flight [12] provide portability, by using a sensor to determine the depth of an object by measuring the time taken by a signal to return to the sensor after reflecting off the target. Unlike CT data, 3D scans provide information only about the outer surface of a specific target.

Since, assessment of medical data (either 2D or 3D) can only be performed after extraction of relevant information from its regions of interest, in our work we employ 2D segmentation techniques for the delineation process in both target applications.

2.2 Medical Image Segmentation

Medical image segmentation is an important step in the extraction and analysis of regions of interest from medical images. The process involves dividing an image into several areas based on a certain rule or description such as intensity level, color value or texture. Several methods on image segmentation using traditional techniques like thresholding, edge detection, and active contours, are presented in works like [13]. One such technique, that is easily applicable to 3D input data, is the iso-contours method.

2.2.1 Iso-Contours

Iso-contours, also known as contour maps, can be used to assess the shape and structure of 3D data. They condense the information from a 3D function representing the input data, over a 2D region of a discrete set of closed lines. Here, the contour lines connect points of equal value known as iso-value [14, 15, 16], thereby delineating/ segmenting them from the rest. Contour maps carry data about measurements taken at specific locations within a defined region of space, such as elevation on a topographical surface (as seen in Fig. 2.2). An example of contour maps applied to craniofacial medical data can be seen in Fig. 2.3, where each contour divides points in the underlying space based on their elevation or iso-value. Such a representation, generated using *Marching Squares*, is used for the fine assessment of regions with varying elevations.

Marching Squares

Marching Squares is a popular algorithm used in the generation of iso-contours [17] within a two-dimensional scalar field (2D array). An overview of the algorithm is shown in Fig. 2.4. Here, contour lines are generated by:
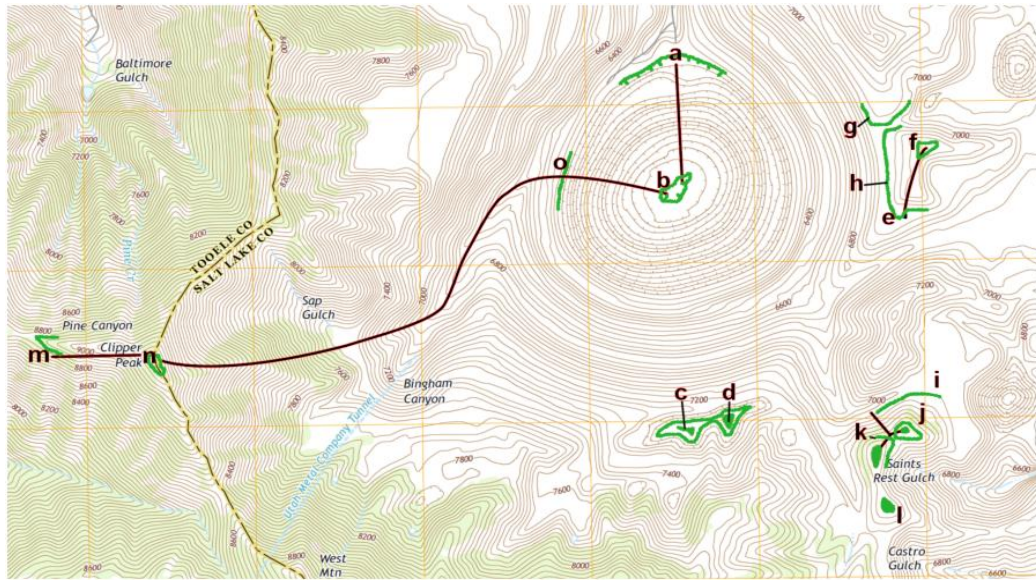
Figure 2.2: Illustration of a contour map, with iso-contours for visualizing the topography [14].
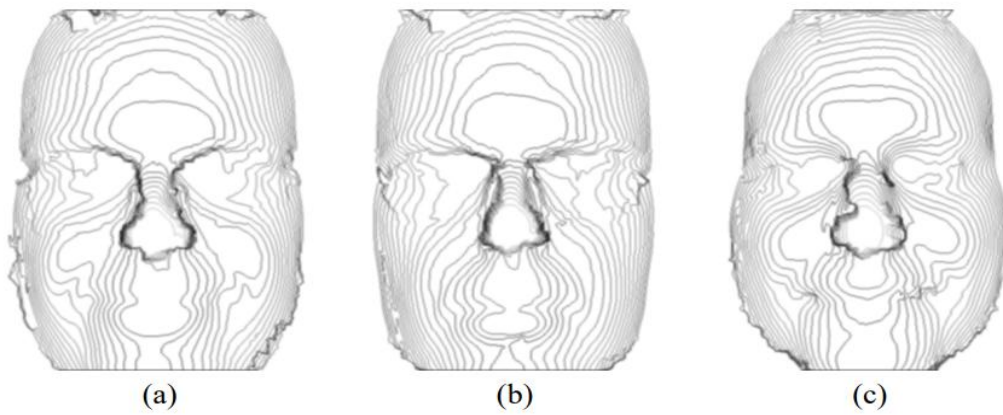
Figure 2.3: Illustration of iso-contours for: (a) and (b) – same person with different expressions; (c) – different person [15].
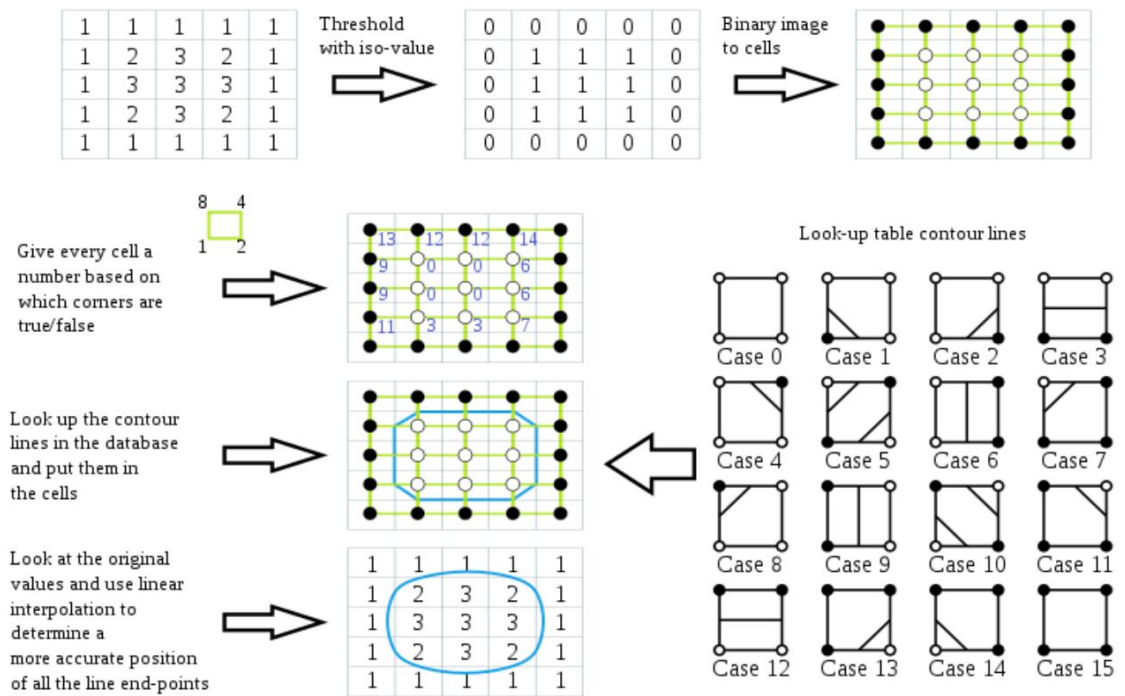
Figure 2.4: Illustration of Marching squares algorithm for generation of contour lines [17].

- applying the iso-value as a threshold to the 2D scalar field, with outputs 1 or 0 corresponding to input data being above or below the iso-value, respectively

- forming contouring cells from the binary image using every $2{\times}2$ block of pixels, for representing the entire image through grid cells

- composing the cell index values using the cell corners as bits resulting in a 4-bit index

- using the cell index to find matching contour lines from a pre-built look-up table

- applying linear interpolation to the 2D scalar values for producing contour lines along the appropriate cell edges

Now applying this algorithm across all iso-values, give us the contour lines that describe the entire topography of the input 3D data, which is useful for further assessment.
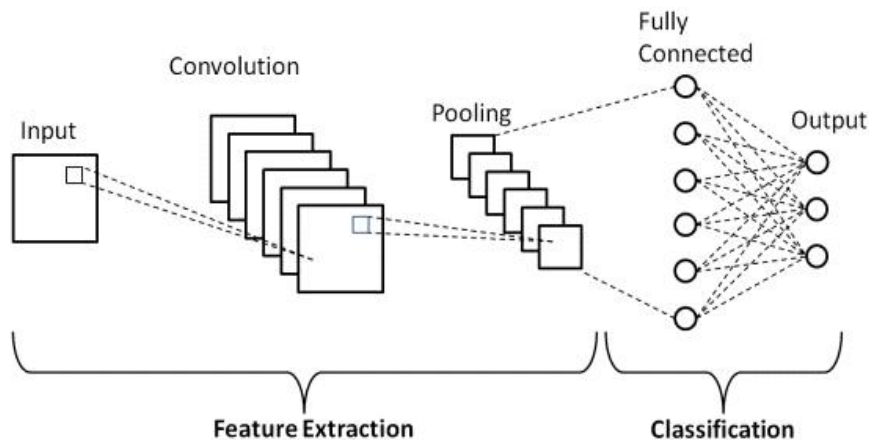
Figure 2.5: Illustration of a typical CNN structure for classification task [23].

Moving on to the assessment of CT data, we again require data delineation/ segmentation for facilitating the analysis of regions of interest. But the traditional techniques like [13] or contours maps [16] produced from intensity-based iso-values, produce segmentation results of poor quality and often require more intervention, due to many constraints. Since machine learning and deep learning-based technologies have demonstrated robustness to such issues, we utilize Convolutional Neural Networks to perform image segmentation on CT data.

2.2.2 Convolutional Neural Networks

Convolutional neural networks (CNNs) today have achieved state-of-the-art performance, especially among computer vision tasks such as image classification [18, 19] and segmentation [20, 21]. This is due to their structure specifically designed for processing 2D spatial data, like images. Since the breakthrough of AlexNet [22] in the 2012 ImageNet competition, CNNs have received serious consideration from the imaging community, leading to constant innovation and development within the field. Unlike traditional methods that rely on rule-based hand-crafted features for vision tasks, CNNs learn feature representations that are robust to image noise, directly from the training data resulting in superior performance. Even with a plethora of different CNN architectures the building blocks usually stay the same [23, 24], and are usually comprised of – convolution layers followed by an activation function, pooling layers and fully connected layers as seen in Fig. 2.5.

Convolutional Layer A convolution layer extracts various features from the input through the

9
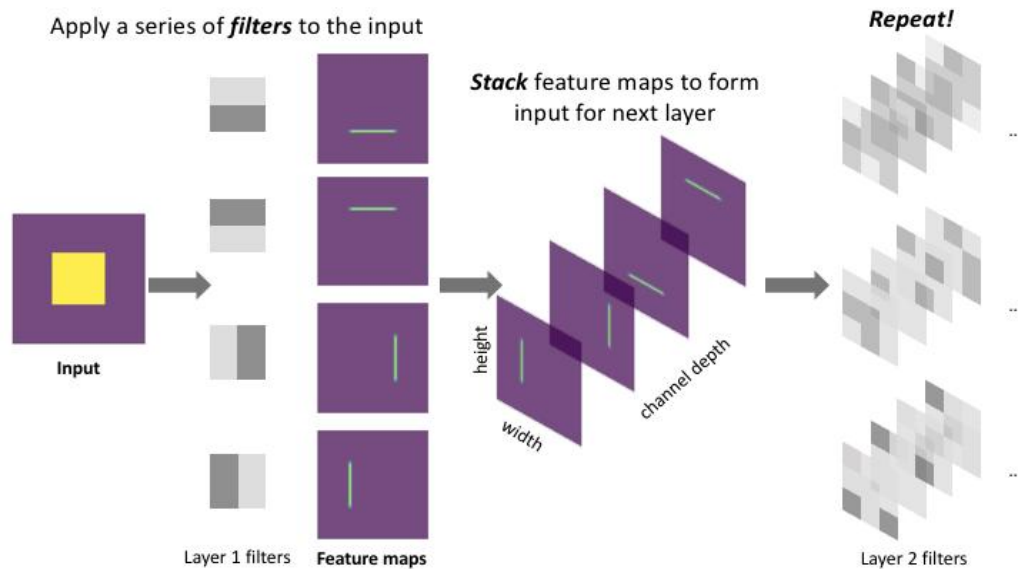
Figure 2.6: Illustration of a feature map generation from convolution operation [24].
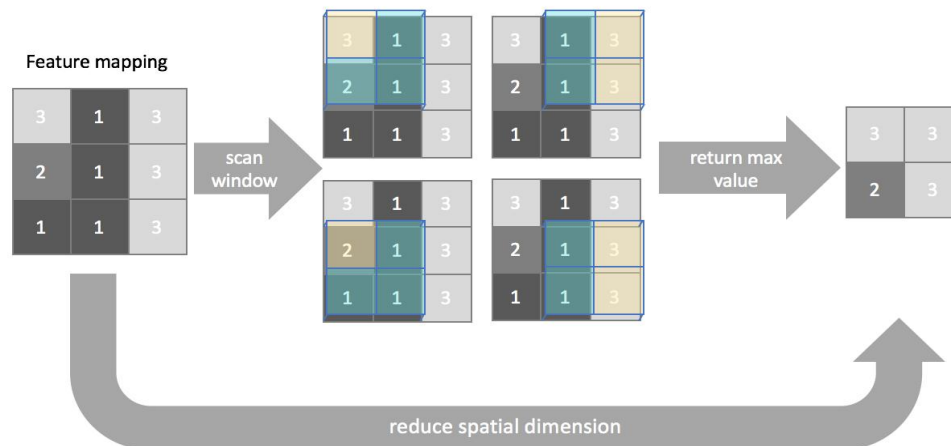
Figure 2.7: Illustration of pooling operation for reducing spacial dimension [24].

convolution operation. It involves using filters or kernels that are used to examine a subset of an image of a particular size M × M. While, a filter is scanned over the entire input image of size N × N, (N > M), a filter response is obtained from the dot product of coefficients between the filter and the corresponding subset of the input. The filter response or the output is commonly known as a feature map as it provides information about the image features like corners and edges, along with their spacial location and orientation. By stacking layers of filters (i.e., convolutions), identifying basic patterns from the initial layers becomes possible as shown in Fig. 2.6.

10

Pooling Layers are commonly used for compressing the information after convolution operation. They down-sample the size of the convolved feature maps, as seen in Fig. 2.7, which reduces the computational cost due to decreased number of parameters. Similar to convolution, pooling requires a filer of a certain size and stride, that scans across the feature map. The two common types of pooling operations are: Max Pooling and average pooling, performed by choosing the largest value and average value, respectively, from a feature map. The outputs from a pooling layer are usually vectorized and sent to the Fully connected layer for a classification task but in the case of segmentation, the feature maps are sent to Fully Convolutional Networks.

Fully Convolutional Networks The Fully Convolution Networks (FCN) approach proposed in [21], replaced the Fully connected layers of a CNN with an FCN before the output layer, thus making the entire CNN architecture fully convolutional. It utilized a classification network like AlexNet [22] as an encoder module for sub-sampling and used a decoder module with transpose convolutional layers for up-sampling. This allows for output feature maps to be recovered at the same resolution of the original input, which is crucial for producing segmentation maps.

CNN based Image Segmentation

CNN approaches like FCN [21], U-Net [20], and V-Net [25] have received a lot of attention from the imaging community for their ability to perform semantic segmentation, and instance segmentation. Since our target application doesn't require the identification of different instances of bones from CT data, we choose to perform semantic segmentation as seen in Fig. 2.8. The purpose of semantic image segmentation is to assign a class to each pixel in an image, corresponding to its representation. This assignment is known as a dense prediction because the CNN is predicting for every pixel in the image, as seen in Fig. 2.9.

Task Representation: In semantic segmentation, we generate a segmentation map (Dimension: height $\times$ width $\times$ 1), from either an RGB color image (Dimension: height $\times$ width $\times$ 3) or a grayscale image (Dimension: height $\times$ width $\times$ 1). Within a segmentation map, each pixel has a class label represented by an integer. The targets are generated by one-hot encoding the class labels, basically generating an output channel for each of the available classes, as seen in Fig. 2.10.

Here, a mask is a single channel from the target (predictions) that illuminates the parts of an
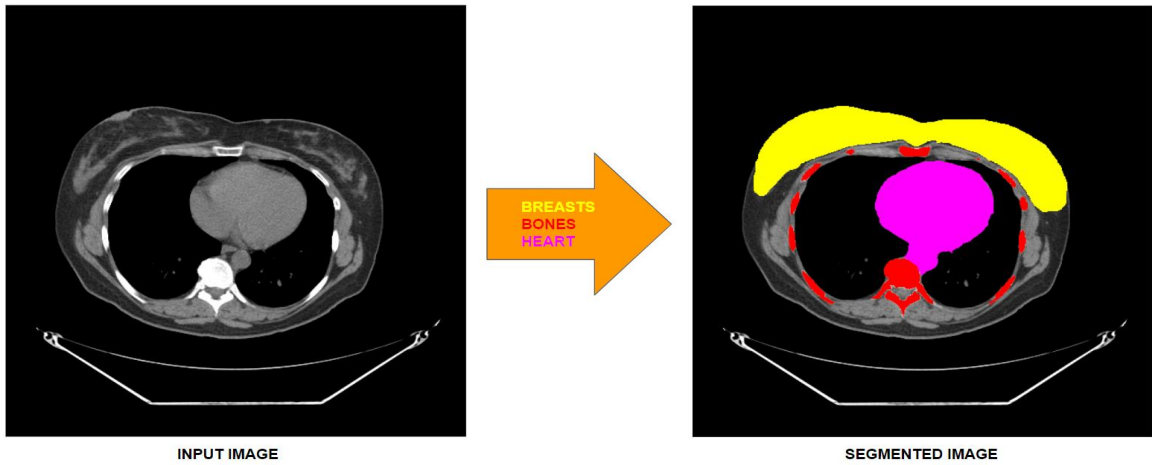
Figure 2.8: Illustration of semantic segmentation for predicting class labels of each pixel in the image.
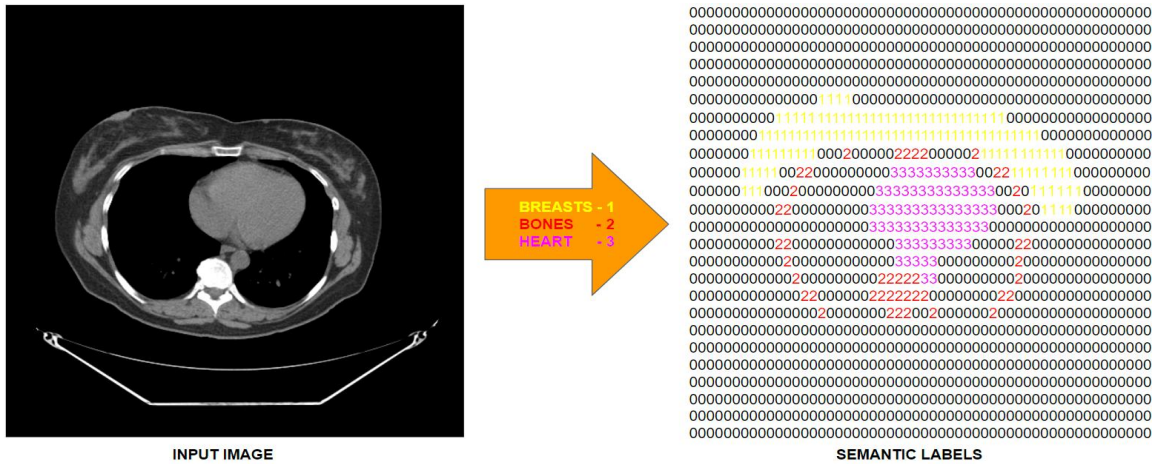
Figure 2.9: Illustration of a prediction map with semantic labels, in low resolution (in practice label resolution will match the input resolution).

image where a specific class is present. This can be inspected by overlaying the target onto the input, as seen in Fig. 2.11.
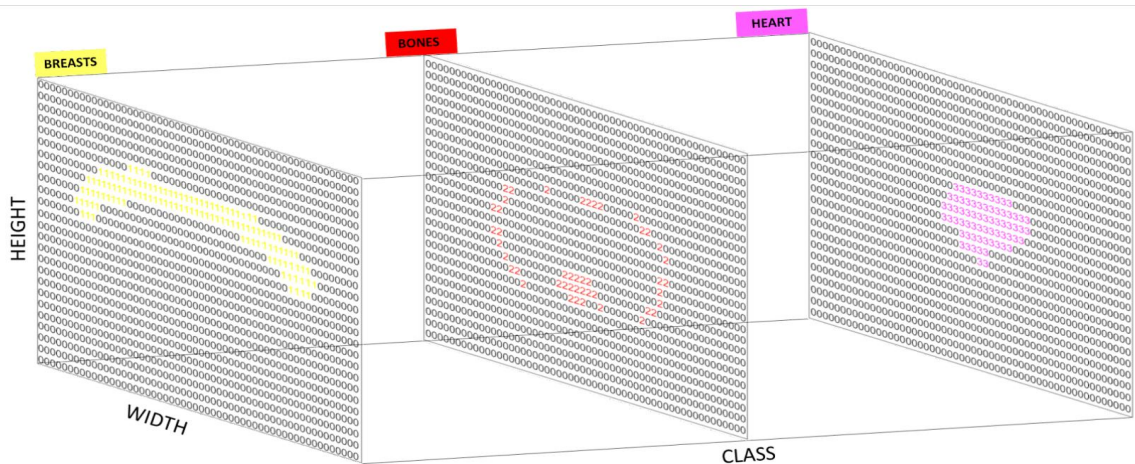
Figure 2.10: Illustration of target channels for each possible class.
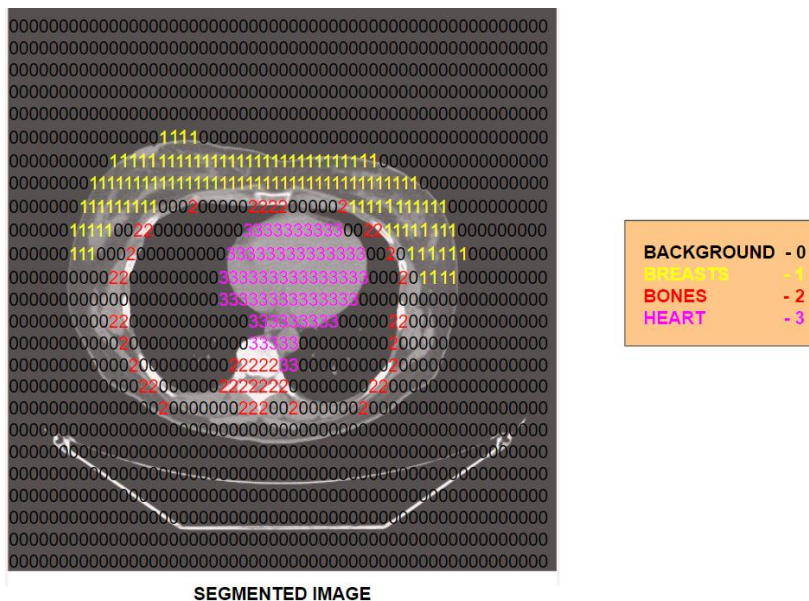
Figure 2.11: Illustration of target inspection through overlay onto input image.

Chapter 3

Boosting Segmentation Performance using Histogram Specification

In this chapter we present our first application of this thesis, which is pelvic bone segmentation for designing pessaries. A version of this chapter was presented at the 2021 IEEE International Conference on Bioinformatics and Biomedicine (BIBM) [1]:

- **Jois PS**, Manjunath A, Fevens T. Boosting Segmentation Performance across Datasets using Histogram Specification with Application to Pelvic Bone Segmentation. In 2021 IEEE International Conference on Bioinformatics and Biomedicine (BIBM) 2021 Dec 9 (pp. 1364-1369). IEEE.

3.1 Introduction

Pelvic Organ Prolapse (POP) [2] is a disorder in which the uterus, rectum or bladder descends into the vaginal canal due to ligament and pelvic muscle weakness [27]. The different stages of POP are showcased in Fig. 3.1. On average one out of ten women around the world will suffer from this ailment [28]. Its reconstructive surgery aims to repair the pelvic floor and restore the position of the organs to their original state. This includes the employment of a vaginal mesh, which has been

---

[2]Warning: the following sections contain graphic images, that some people may find disturbing.

14
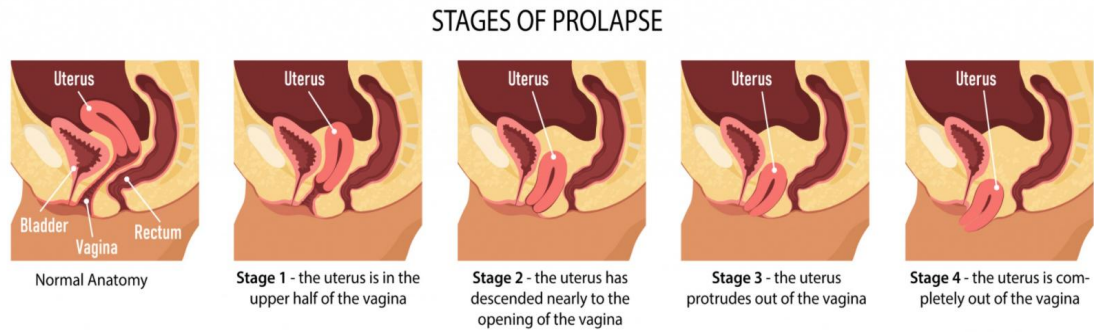
STAGES OF PROLAPSE

Figure 3.1: Illustration of different stages of pelvic organ prolapse [27].

linked to several medical problems and has been the subject of several lawsuits previously [29]. The latest clinical therapy for POP is an intravaginal device called Pessary [30], which suffers from a failure rate of 40% due to its generic form, which is also not a good match to the female pelvic anatomy, as shown in Fig. 3.2. Its poor design and performance are a result of the limited data on patient-specific pelvic anatomy. Here, segmentation of pelvic bone becomes key to extracting patient-specific anatomical measures, that aid in designing patient-specific pessaries [26].

In this context Computerized tomography (CT) imaging becomes crucial as it aids in the clinical diagnosis of diseases and planning of pelvic surgeries. Several methodologies have been proposed for the segmentation of the pelvis with the emergence and advancements of deep learning for digital healthcare. But in a low data scenario, the lack of abundant data needed to train a Deep Neural Network is a significant bottleneck. Due to this, boosting the performance of networks trained on limited data through *Radiomics* becomes essential for accurate segmentation of the pelvis.

The automated results from the segmentation task injects digitized data into the decision making process and aid physicians in the early detection of pelvic injury, which expedites surgical planning and helps to reduce the complications caused by pelvic fractures [31]. In pelvic CT data, structures like the bone marrow and bone surface relatively appear as dark and bright regions due to their low and high densities compared to the surrounding tissues. However, given the variations in image brightness and contrast between different CT datasets, as illustrated in Fig. 3.3, distinguishing pelvic bone structures from the image background becomes cumbersome and leads to erroneous segmentation outputs. These issues indicate a need for a novel solution to develop a simple yet effective methodology for the accurate segmentation of pelvic bones from varying CT data.

15
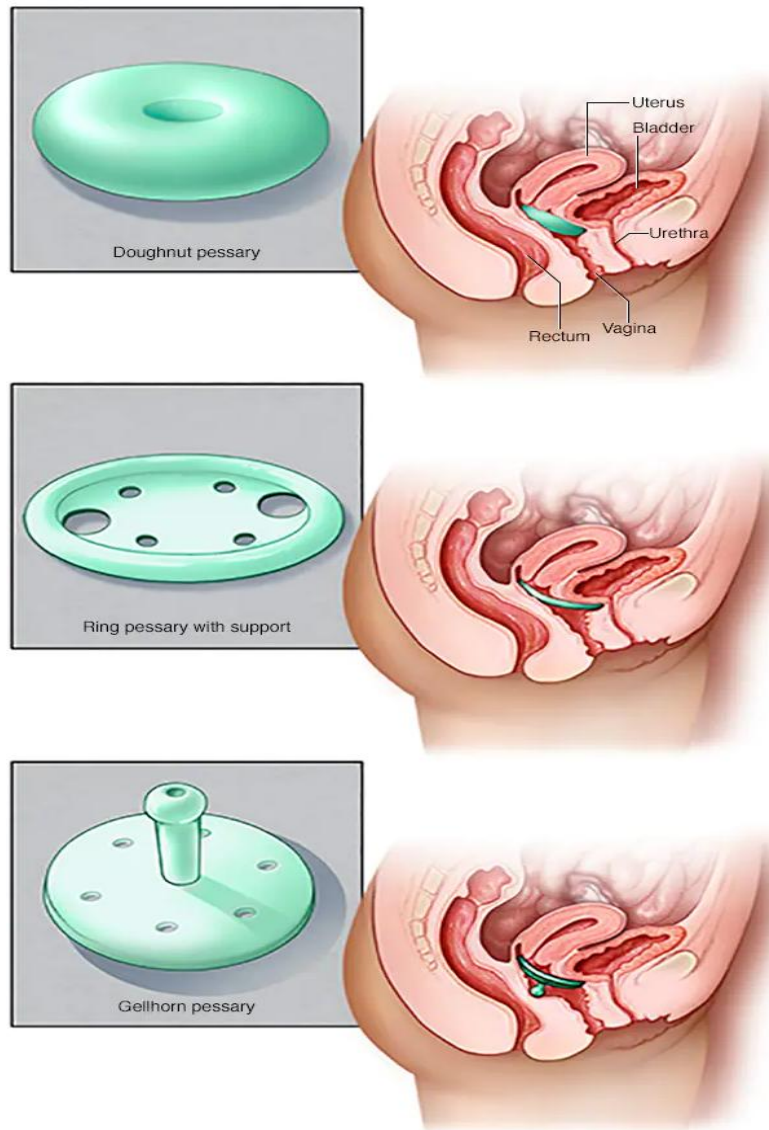
Figure 3.2: Illustration of different pessaries with generic shapes [30].
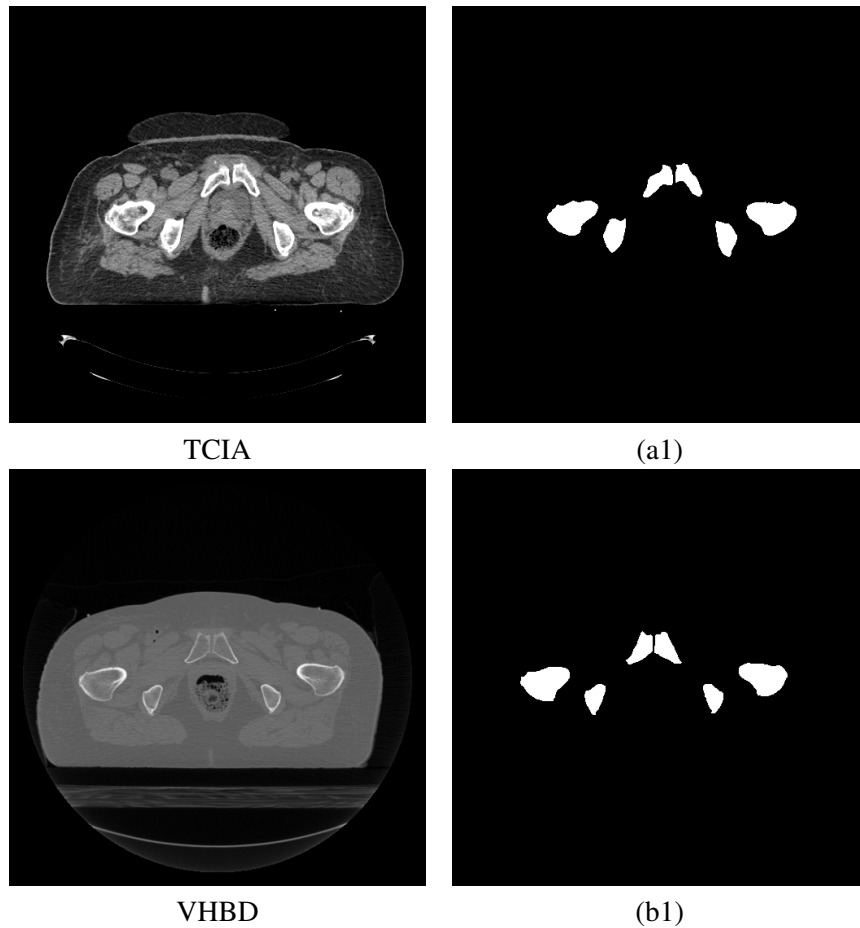
Figure 3.3: (a1) and (b1) – illustrate the segmentation outputs, for input images from TCIA and VHBD, respectively.

Recent literature has seen many applications for the segmentation of the pelvis from CT imaging data. Traditional methods such as thresholding and region growth [32], deformable surface model [33], and others, have been commonly used to perform bone segmentation. However, these approaches often suffer from low accuracy due to varying image properties such as intensity, contrast, and the inherent variations between the texture of the bone structures (bone marrow and surface boundary) and the surrounding tissues. To overcome these challenges, supervised methods such as statistical shape models (SSM) and atlas-based deep learning (DL) methods have made significant contributions to segmentation tasks. Wang *et al.* [34, 35] suggested using a multi-atlas segmentation with joint label fusion for detecting regions on interest from CT images. Yokota *et al.* [36] showcased a combination of hierarchical and conditional SSMs for the automated segmentation of
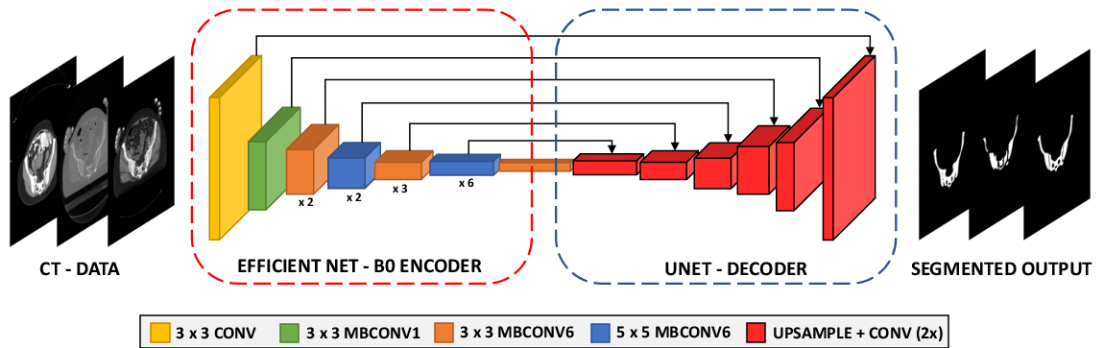
Figure 3.4: Workflow of U-Net architecture with pre-trained backbone, detailing pelvic bone segmentation.

diseased hips from CT data. Chu *et al.* [37] presented a multi-atlas based method for accurately segmenting femur and pelvis. Zeng *et al.* [38] proposed a supervised 3D U-Net with multi-level supervision for segmenting femur in 3D MRI. Chen *et al.* [39] showcased a 3D feature enhanced network for quickly segmenting femurs from CT data. Chang *et al.* [40] proposed patch-based refinement on top of a conditional random field model for fine segmentation of healthy and diseased hips. Liu *et al.* [41] used 3D U-Nets in two-stages (trained on approximately 270K images) with a signed distance function for producing bone fragments from image stacks. In the following section, we discuss a new technique addressing accurate segmentation of the pelvis from CT images of varying qualities.

3.2 Proposed Methodology

The efficacy of using Encoder-Decoder architectures for designing high accuracy segmentation models for biomedical applications has been showcased in recent literature [20, 38, 41]. We employ a similar architecture, with various encoder modules for feature extraction and a decoder module for semantic segmentation. The details of the encoder and decoder modules are explained in the following.

18

3.3 Prior Art

3.3.1 Encoder Module

In simple terms, an encoder takes the input image and generates a high-dimensional feature vector aggregated over multiple levels. We deploy a choice of the following well-known architectures as the encoder module:

ResNet

Residual networks (ResNet) introduced residual mappings to solve the vanishing gradient problem in deep neural networks [18]. ResNets are easy to optimize and gain accuracy even with deeper models.

Inception V3

Inception Networks are computationally efficient architectures, both in terms of the model parameters and their memory usage. Adapting the Inception network for different applications while ensuring that changes do not impede its computational efficiency is difficult. Inception V3 introduced various strategies for optimizing the network with ease of model adaptation capabilities [19].

EfficientNet

Conventional methods make use of scaling to increase the accuracy of the models. The models are scaled by increasing the depth/width of the network or using higher resolution input images. EfficientNet results from a novel scaling method that uses a compound coefficient to uniformly scale the network across all dimensions [42].

3.3.2 Decoder Module

The decoder module is responsible for generating a semantic segmentation mask using the aggregated high-dimensional features extracted by the encoder module. We make use of the popular U-Net model specially designed for medical imaging as the decoding module [20].

3.3.3 Histogram Specification

Histogram specification, or histogram matching, is a traditional image processing technique [43] that matches the input image's histogram to a reference histogram. Histogram specification involves computing the cumulative distribution function (CDF) of histograms from both the target and the reference, following which a transformation function is obtained by mapping each intensity level from the target's CDF to the level in the reference CDF as shown below,

1. we compute the CDF $T(r_k)$ from the input's histogram equalized transformation,

   $T(r_k) = (L-1) \sum_{i=0}^{k} p_r(r_i) = \frac{(L-1)}{MN} \sum_{i=0}^{K} n_i$

2. we then compute the transformation function for the output, $G(z_q) = (L-1) \sum_{j=0}^{q} p_z(z_j)$

3. for all $T(r_k)$ we find the closest corresponding values in $G(z_q)$ from Step 2

4. If more than one z_q satisfies $T(r_k) = G(z_q)$, we choose the smallest value and store all the mappings from r to z, through the inverse transform $z_q = G^{-1}(T(r_k))$.

5. using values from Step 4, we map every histogram equalized pixel from the reference, $T(r_k)$, to the corresponding z_q of the target's equalized histogram

where, r and z are the intensity levels of input (reference image) and output(target image); $k = q = 0, 1, 2, ..., L-1$; L is number of possible intensity levels; MN is number of image pixels; n_i is number of pixels with intensity r_i;

In this work, we construct the reference histogram from the training set and use it to modify (pre-process) the test data, before performing the segmentation task(Shown in Sec. 3.4.3).

3.3.4 Datasets

The input data preparation and label annotation were done using the tools from *Image-J* software [44]. A summary of TCIA–cancer imaging archive [45] and VHBD–Visible human project [46] datasets, its image resolution, number of images used in this study, and the respective data-splits for training-validation-testing, are shown in Table 3.1.

Table 3.1: An overview of the datasets used in this work.

Dataset	Resolution # Images	Train-set (%)	Val-set (%)	Test-set (%)
TCIA [45]	512 x 512 582	407 (70%)	58 (10%)	117 (20%)
VHBD [46]	512 x 512 167	–	–	167 (100%)
VHBD-2 [46]	512 x 512 167	116 (70%)	17 (10%)	34 (20%)

3.3.5 Performance Measures

To quantify the quality of segmentation, we compute standard performance measures for segmentation tasks commonly used in literature, specifically, the mean Dice coefficient (mDice) and mean Intersection over Union (mIoU) [47, 48]. For a given segmentation output (A) and the ground truth (B), the Dice coefficient is given by Dice $= \frac{2|A \cap B|}{|A| + |B|}$, which can be interpreted as a weighted average of the precision and recall, and IoU $= \frac{|A \cap B|}{|A \cup B|}$, (also known as Jaccard index) is commonly used for comparing the similarity between sets (A) and (B), while penalizing their diversity.

3.4 Experimental Validation

3.4.1 Network Training

The network implementations were based on the documentation from [49]. The encoder module pre-trained on the ImageNet [50] dataset was employed to improve the generalization capability on unseen data and achieve faster convergence. For the base-model, we use ResNet-34 [18] as the encoder and a U-Net decoder. We initialize the base-model with random weights (**rnwt**) and train without any data-augmentation (**noaug**) on images from [45], using an Nvidia RTX 2070 GPU, and an ADAM optimizer with a learning rate of 0.001, momentum of 0.9 and a weight decay of 0.0001, for 40 epochs. We chose a 70% : 10% : 20% split of the data (shown in the first row of Table 3.1), where the 70% was utilized for training and the 10% of the data was utilized for validation. The remaining 20% for testing was completely unseen during training. About 50 passes of random

21

image batches, of size eight, from the training set, were used in each epoch. The model was then validated on the 10% data to evaluate the performance based on binary-cross-entropy loss (**BCE**) and record the corresponding weights. After training, the weights that gave the best performance on the validation set were selected for the base-model, which was then evaluated on the unseen test-sets, i.e., 20% of [45] and 100% of [46], respectively. The base model's performance is showcased in the first row of Table 3.2.

Extending beyond the base-model, data augmentation (**aug**) was performed using horizontal and vertical flips, affine transforms, image intensity modulation and blurring, for increasing training data size and to help reduce over-fitting. In addition, we try to find the best overall segmentation performance and generalization capability to completely unseen data, through further extension of the base-model with different configurations, using the following:

- *encoder modules* using ResNet-34 [18], Inception V3 [19] and EfficientNet-B0 [42], initialized with ImageNet weights (**imwt**) for transfer learning

- *re-configuration* of input data, or not, to the pre-trained model's format and its pre-processing functions (**ppr**), for extraction of better features

- *loss functions* like **Dice** loss, **IoU** loss and combined **BCE-IoU** loss, in place of **BCE** loss (seen below), for propagating strong gradients for better optimization and learning

$$\mathcal{L}_{BCE}(y, \hat{p}) = -(y * log(\hat{p}) + (1 - y) * log(1 - \hat{p})) \tag{1}$$

$$\mathcal{L}_{Dice}(y, \hat{p}) = 1 - \frac{2y\hat{p} + 1}{y + \hat{p} + 1} \tag{2}$$

$$\mathcal{L}_{IoU}(y, \hat{p}) = 1 - \frac{y \cap \hat{p} + 1}{y \cup \hat{p} + 1} \tag{3}$$

$$\mathcal{L}_{BCE\,IoU} = \lambda\,BCE + (1 - \lambda)\,IoU \tag{4}$$

In equations (1) to (3) y is the ground-truth and $\hat{p}$ is the model prediction. In (2) and (3) we ensure that the functions are not undefined when $\hat{p} = y = 0$, by adding 1 to the numerator and denominator. And in (4) we use a convex combination of BCE and IoU losses, where λ was set to 0.5.

3.4.2 Results

The detailed comparisons of the different U-Net configurations' segmentation performance on test-sets with 95% confidence intervals are shown in Table 3.2. The segmentation outputs from both, the *least-performing* (base-model) and the *best-performing* (seen in Fig. 3.4, a fine-tuned U-Net configuration with EfficientNet-B0 encoder [42] pre-trained on ImageNet, with data-augmentation and input re-configuration, optimized using augmented BCE-IoU loss) DL models, are showcased in Figs. 3.5 (a) &(b). The predicted outputs are overlaid onto the ground-truth and color-coded (yellow - TP; black - TN; green - FP; red - FN) for visualizing the quality of segmentation. The results shown in Figs. 3.6(b2) &(c2) illustrate the desired effect on segmentation due to histogram specification. The reduction in the number of pixels labelled as FPs & FNs, and improvement in the number of TPs from the overlays decisively show the significance of pre-processing test-data, which boosts the model's segmentation performance. Furthermore, the comparative results tabulated in the last two columns of Table 3.2, along with the two sample t-test for the mean dice coefficient (**mDice**) between the best model (✰) and every other model configuration, on the histogram matched test data (proposed methodology), gives evidence for the statistical significance of the proposed method with the exception of a U-Net configuration with Inception Net-V3 encoder [19] pre-trained on ImageNet, with data-augmentation and input re-configuration, optimized using BCE loss function.

3.4.3 Discussion

Since EfficientNet is a state-of-the-art, the optimized network that achieved superior results on the ImageNet dataset, with a relatively small number of the trainable parameters due to the compound scaling approach [42], choosing it as the encoder module yields superior segmentation performance compared to other configurations.
For histogram specification, since one needs only a single reference histogram, we take a clustering

| Input | (a) | (b) |
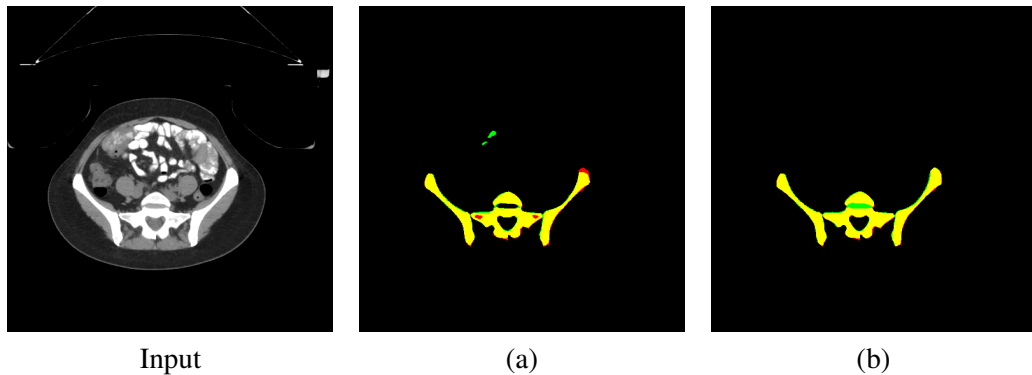
Figure 3.5: Pelvic bone segmentation on TCIA data using: (a) Base U-Net with random weight initialization for ResNet-34 encoder, with no data-augmentation, optimized using BCE loss (**least performing**); and (b) fine-tuned U-Net with ImageNet weight initialization for EfficientNet-B0 encoder, with data-augmentation and input reconfiguration, optimized using combined BCE-IoU loss (**best performing**), are overlaid onto the binary ground-truth; yellow - TP; black - TN; green - FP; red - FN.

approach and choose the cluster centre from all the feature vectors (histograms) of the training set. Since the cluster centre is the mean of all cluster points (vectors), we compute the average histogram from the entire training set as the reference. Using histogram specification as a pre-processing step for the test data serves an important purpose, as it converts the distribution of the test data into a form seen by the network during training, as shown in Figs. 3.6(a1) to (c1). Due to the lack of access to large datasets, the proposed method was validated on the datasets that were available during the experimentation phase.

On analyzing the data shown in Table 3.3, the proposed methodology's overall performance on the test-sets surpassed several state-of-the-art techniques that were trained on similarly sized datasets, except for Liu *et al.* [41] who performed training on approximately 270,000 images. Since data drives any model, the proposed methodology (trained only on 407 images) shows room for further improvement in segmentation under the availability of larger datasets.

3.4.4 Ablation Study

Images from [45, 46], with the data splits shown in rows 1 and 3 of Table 3.1, are used for training. The *best-model* was trained on the joint data whose test-data performance is shown in Table 3.2 (♣). The results showed that training the model on joint data degrades the performance on both datasets. The data imbalance and the varying image tonal distributions play a significant

24

TCIA   (a1)   (a2)

Count: 262144   Min: 0
Mean: 28.801   Max: 255
StdDev: 60.856   Mode: 0 (189971)

VHBD (target)   (b1)   (b2)

Count: 133956   Min: 0
Mean: 42.070   Max: 244
StdDev: 50.752   Mode: 0 (43048)

H-VHBD   (c1)   (c2)

Count: 133956   Min: 0
Mean: 24.589   Max: 254
StdDev: 49.017   Mode: 0 (87658)
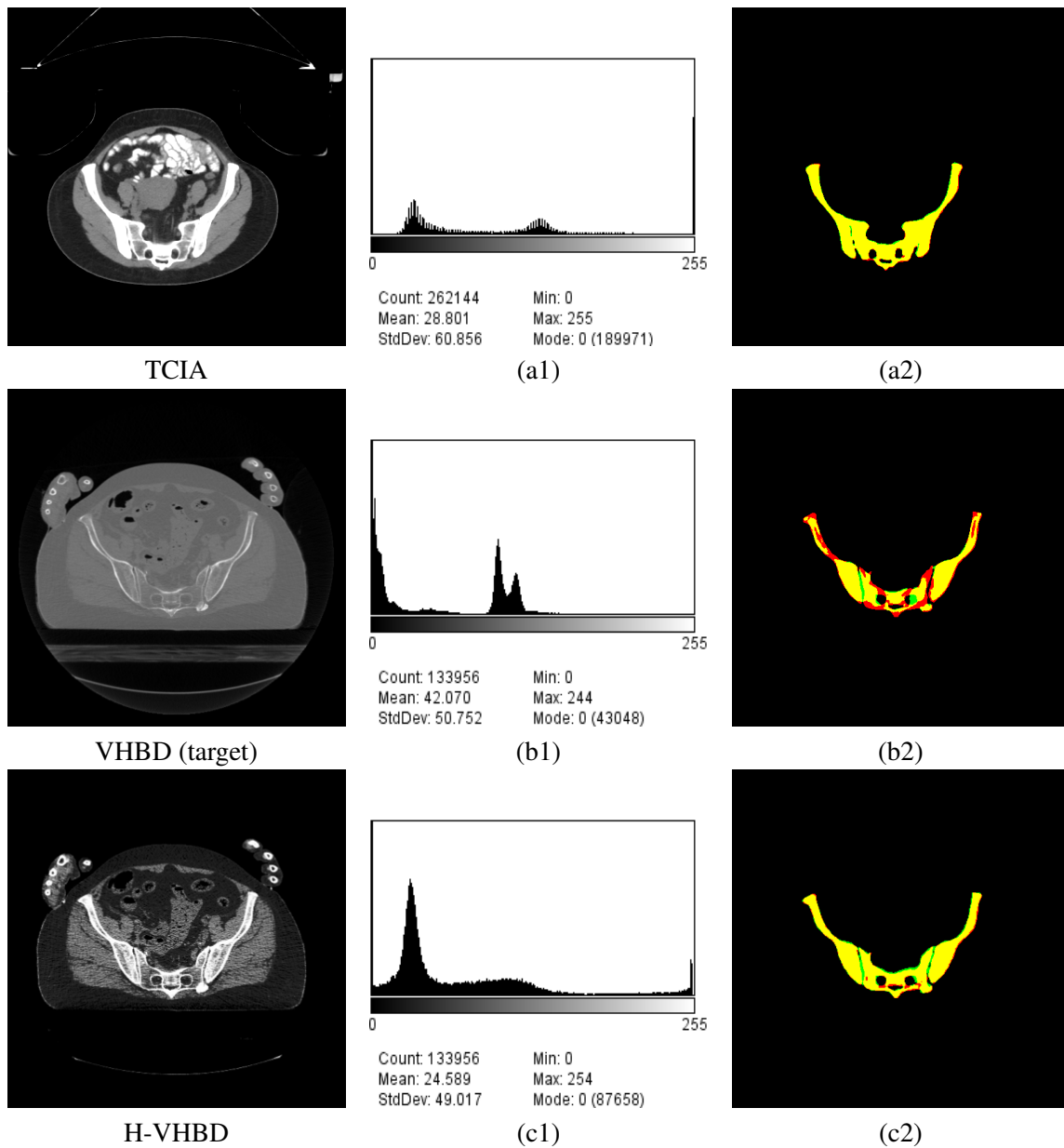
Figure 3.6: Performance in segmentation with histogram specification: (a1-c1) show the respective histograms of the input images; (a2-c2) show the pelvic bone segmentation overlaid on the ground-truth; and (b2-c2) decisively show the improvement in segmentation from matching target's histogram to the reference. yellow - TP; black - TN; green - FP; red - FN.

25

Table 3.2: Performance comparison of different U-Net configurations, with 95 % confidence intervals, for pelvic bone segmentation on test sets from **TCIA**, **VHBD**, and **H-VHBD**, i.e., VHBD after histogram specification. Along with p-value for showcasing the statistical significance of best performing model against other configurations.

U-Net Configurations	TCIA		VHBD		H-VHBD		p-value
	mIoU	mDice	mIoU	mDice	mIoU	mDice	(☆ v/s)
Res34-rnwt-noaug-bce (*base model*)	0.788 ± 0.033	0.867 ± 0.025	0.131 ± 0.033	0.186 ± 0.037	0.774 ± 0.021	0.865 ± 0.015	< 0.001
Res34-imwt-aug-bce	0.919 ± 0.007	0.957 ± 0.004	0.746 ± 0.028	0.840 ± 0.021	0.900 ± 0.004	0.947 ± 0.002	< 0.001
Res34-imwt-aug-dice	0.925 ± 0.007	0.960 ± 0.004	0.523 ± 0.039	0.645 ± 0.038	0.907 ± 0.005	0.951 ± 0.002	0.043
Res34-imwt-aug-bce-iou	0.922 ± 0.007	0.959 ± 0.004	0.790 ± 0.018	0.877 ± 0.012	0.906 ± 0.004	0.950 ± 0.002	0.008
IncepV3-imwt-aug-bce	0.876 ± 0.012	0.932 ± 0.007	0.663 ± 0.026	0.784 ± 0.019	0.906 ± 0.006	0.950 ± 0.003	0.032
IncepV3-ppr-imwt-aug-bce	0.921 ± 0.011	0.957 ± 0.007	0.808 ± 0.014	0.890 ± 0.009	0.913 ± 0.005	0.954 ± 0.002	0.612
IncepV3-ppr-imwt-aug-iou	0.921 ± 0.011	0.957 ± 0.006	0.757 ± 0.019	0.856 ± 0.013	0.901 ± 0.008	0.947 ± 0.004	0.004
EffiB0-imwt-aug-bce	0.923 ± 0.007	0.959 ± 0.004	0.835 ± 0.015	0.906 ± 0.010	0.901 ± 0.006	0.947 ± 0.003	< 0.001
EffiB0-ppr-imwt-aug-bce-iou (☆)	**0.924 ± 0.008**	**0.960 ± 0.004**	**0.836 ± 0.011**	**0.909 ± 0.006**	**0.914 ± 0.005**	**0.955 ± 0.002**	—
ABLATION STUDY (♣)	0.913 ± 0.007	0.954 ± 0.004	0.679 ± 0.047	0.801 ± 0.032	0.873 ± 0.013	0.931 ± 0.007	< 0.001

[*] **Encoder module** - Res34, IncepV3, EffiB0 are ResNet-34, Inception Net-V3, EfficientNet-B0, having 24.43 M; 29.89 M; and 10.07 M (M - Million) number of trainable parameters, respectively.

[*] **Encoder Weights** - rnwt and imwt are random weights and Imagenet weights, respectively.

[*] **Augmentation** - aug and noaug means training with and without data-augmentation, respectively.

[*] **Loss** - bce, dice, iou are the Binary Cross Entropy loss, Dice Loss and IoU loss, respectively.

[*] **ppr**- configure input to the pre-trained backbone's format.

[*] Grey background - indicates improvement due to histogram-specification based pre-processing.

[*] **p-value**- two sample t-test for the mean dice coefficient (**mDice**) between best model (☆) and every other model configuration, on the histogram matched test data (proposed methodology).

Table 3.3: Overall performance comparison for pelvic bone segmentation with state-of-the-art techniques.

Methodology	Dataset (# Test Images)	mIoU	mDice
Yokota et al. [36]	Private (100)	—	0.928
Chu et al. [37]	Private (318)	—	0.941
Chang et al. [40]	Private (~3420)	—	0.949
Liu et al. [41]	DS‡(~63K)	—	**0.984**
Proposed method	TCIA,VHBD (284)	0.919	0.957

(DS‡) KITS19, CERVIX, ABDOMEN, MSD T10, COLONOG, CLINIC; Train:Test $\approx$ 270K: 63K; K = 10^3

role in influencing the segmentation performance. And by using the proposed methodology, the model overcomes data imbalance and generalizes well to unseen datasets, which boosts its overall segmentation performance.

3.5 Conclusion

In this chapter, we showcased a novel methodology for the automated segmentation of pelvic bones from axial CT images. We addressed the unmet need for superior pelvic bone segmentation methodology for images with varying brightness and contrast by using histogram specification. This simple yet powerful approach to pre-processing the test-data improved segmentation performance by a significant margin, with the quantitative results confirming its validity. Through our approach, the encoder-decoder configuration overcame a significant hurdle of varying intensity distributions in CT images, which led to superior segmentation quality. Moreover, after validating the results on publicly available TCIA and VHBD datasets, the proposed methodology is highly competent with-respect-to existing state-of-the-art techniques. Lastly, the segmentation outputs from particular sections of the female pelvic bone (*proprietary information under a Non Disclosure Agreement with FemTherapeutics Inc.*), were processed for computing the patient-specific anatomical features and producing a shape-prior (*dependent on the accuracy of segmentation output*), that was highly useful in designing patient-specific customizable pessaries.

Chapter 4

VIMA

In this chapter, we introduce **V**olumetric and **I**so-contour based **M**orphological **A**symmetry (**VIMA**) score and visualization scheme [1] [2], for the quantitative and qualitative assessment of breasts in 3D [51]. The acronym was inspired by the Sanskrit word " Vimā " meaning: *dimension, measure out* and *make ready*. The proposed method (a quantitative metric and visualization scheme) is aimed at *making ready* the hard to obtain digital information of the breast(s) *measured* in an intra and perioperative setting, for increasing the observer's *dimension* for decision making, which has a profound impact on the outcome of aesthetic breast surgeries.

4.1 Introduction

One of the standard approaches for treating breast cancer today is a mastectomy [52], the complete surgical removal of the breast tissue, as shown in Fig 4.1. This invasive procedure, although life-saving, is commonly known to have a profound negative impact on a breast cancer survivor's emotional well-being, body image, and quality of life [53]. Due to this, the present-day treatment for breast cancer encompasses the removal of cancerous tissue and the surgical reconstruction and modification of the breast(s) to a form that appears satisfying to the patient [54]. Despite the growing demands for aesthetic and reconstructive breast surgeries, until recent times, the breast morphology and the reconstruction outcomes were evaluated purely via naked eye assessment and simple
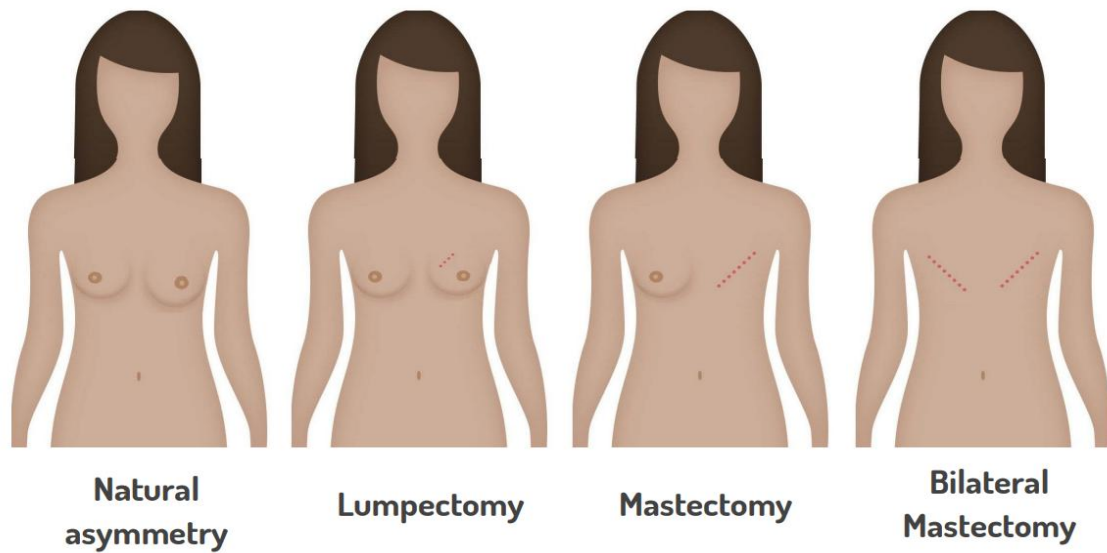
Figure 4.1: Illustration of natural and surgically induced breast asymmetry.

anthropometry (tape measurements). Even with the availability of photogrammetry and hand-held 3D depth sensing, there is a dearth of fully automated commercially available perioperative (pre, intra, and postoperative) assessment techniques that can assess patients' breast surface and volume [55, 56]. While most existing methods for automated assessment of breasts rely on 3D data obtained from time-of-flight sensors on any standalone or hand-held 3D scanners, their reliance on linear-measurements disables them from capturing important data from the entire breast mound. In this work, we propose a methodology using *Radiomics* for providing: (a) 3D visualization and location of the regions that contribute to the overall asymmetry; (b) type of asymmetry; and (c) the exact quantity of a specific type of asymmetry, between the two breast contours, for aiding plastic surgeons in reducing the incidence of breast asymmetry during aesthetic breast surgeries.

4.2 Background

According to the World Health Organization, breast cancer is the most common form of cancer, affecting one in every eight women in North America. In 2018 alone the estimated mortality due to breast cancer was over 600,000 [57]. Treatment for breast cancer is normally dependent on the type of cancerous tissue and its stage. It usually involves chemotherapy, invasive surgery, and/or
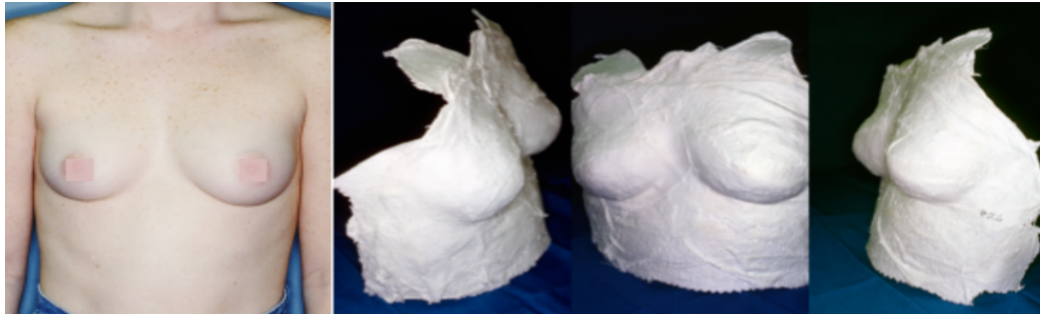
Figure 4.2: Plaster cast of the torso for quantifying breast morphology from the mold [58].

radiation therapy. A common method used to remove existing cancerous tissue, and reduce the chance of developing cancer in the future is prophylactic mastectomy. Here, one or both breasts are usually removed in order to reduce the risk of development or recurrence of breast cancer [52].

Studies like [53] have provided compelling evidence for the negative effects of procedures like mastectomy on a breast cancer survivor's quality of life, body image and emotional well-being. Hence, breast reconstructive surgery is an important component of the treatment process, for improving a patient's self-esteem. Here, reconstructive surgeries are typically performed to improve the patient's breast morphology, described in terms of shape, size, position, symmetry and appearance [54], but any dissatisfaction with the surgical outcome results in revision (additional surgeries). During any revision, a surgeon will try to modify the post-reconstructive breast morphology until the patient is satisfied with the outcome. For any given reconstructive or revision procedure the final result is heavily dependent on a surgeon's experience and ability to predict the outcome, based on naked-eye assessment and qualitative evaluation of the patient's breast morphology.

Although there has been a growing interest in the usage of an objective and quantitative assessment of breast morphology, it is dependent on direct anthropometry, or manual tape-based measurements like [55, 56]. Another common manual technique is the use of mesh/plaster cast [58] (shown in Fig. 4.2). This involves physically pressing a cast against the subject's torso area in a careful manner to procure an inverted mould of the torso. The inverted mould is used to quantify the subject's breast morphology. However, the use of a mesh/plaster case is both time consuming and non-feasible during surgery. Techniques like [58, 59] include the use of the water test. In a
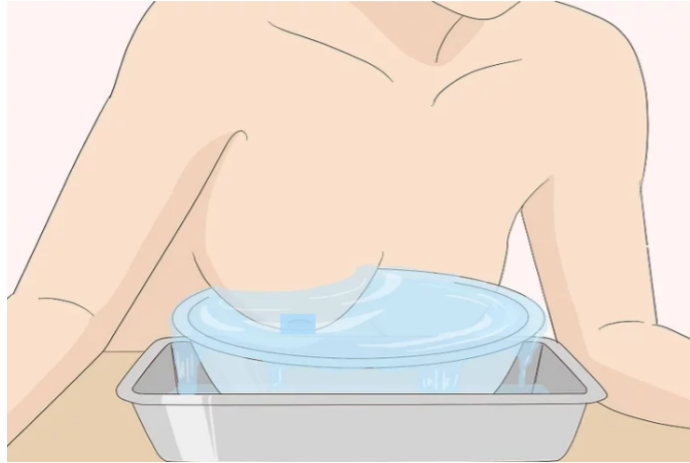
Figure 4.3: Water displacement test for estimating breast volume [59].

water test, the subject's breast mounds are individually inserted into water containers. The approximate volume of the breast is determined based on the amount of water displaced from the water container (as shown in Fig. 4.3). This test, is both impractical in a real life setting during and after surgery, and can only provide volumetric measurements, without any information on the shape and position of the breast mounds.

Due to the advancements in medical image processing and computer vision, techniques like 3D scanning through image-photogrammetry have found their use in the morphological assessment of breasts during surgical planning [58, 60, 61]. Their non-invasive nature makes data acquisition and processing relatively easy and makes it possible to compute approximate values for breast measurements, size and volume [62, 63, 64]. But they are not fully automated as the landmark points have to be entered manually into the software tool by trained personnel, before performing any assessment, similar to [65]. The linear measurement based assessment methodologies in [66, 67], not only requires manual intervention for selecting the landmark points before producing the linear measurements but its assessment methodology was performed on scans from the Vectra system by Canfield, which is known to consume a lot of time before producing 3D data of the patient's breasts, as it employs photogrammetry for data acquisition (issues confirmed by the authors of [66]) .

Works like [67, 66] are not feasible in an intraoperative setting due to manual intervention for landmark annotation, and the lack of portable 3D scanners [68] and [69], respectively, as they suffer from the inability to capture the intraoperative data needed for assessment, while the patient is in
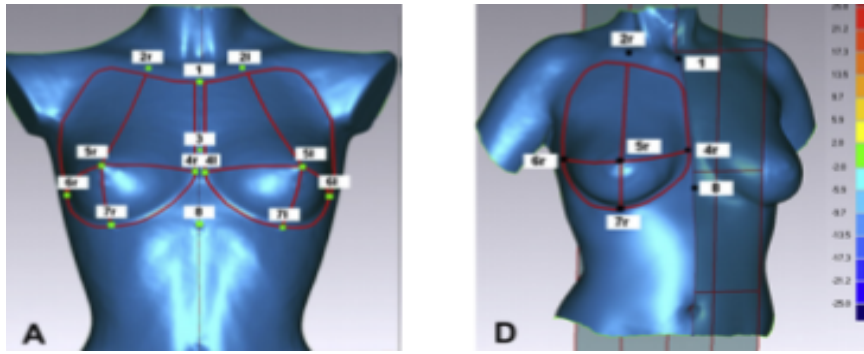
Figure 4.4: Illustration of breast symmetry assessment using BCCT score [65].

a supine position. The works proposed in [70] can capture the necessary patient data even from the supine position, but like the previous works, don't quantify breast dissimilarity in an automated fashion. And while, the work proposed by S. Amini et al., [71], showcases a combination of Finite Element Analysis and AR visualization for performing breast symmetry assessment, it fails to quantify the exact position and amount of breast tissue needed to improve the overall symmetry. This method is also not contact free, as it needs a special marker that is placed in contact with the patient's breast, for aiding data calibration and localization, which reduces its overall clinical utility during surgery.

Today the state of the art methods [65, 66, 67], for performing a digital assessment of breast morphology (seen in Figs. 4.4, 4.5 and 4.6, respectively), still rely on linear measurements to describe the breast morphology and ascertain their dissimilarity, without taking into account the entire 3D surface of the individual breast mounds. This leads to the loss of useful information that is critical for making real-time adjustments during breast surgeries. And due to the lack of such information, the surgeons still have to rely on their naked eyes for guessing the amount of dissimilarity in volume and shape, between the two breasts, during surgery.

4.3 Proposed Methodology

We propose **VIMA**, (**V**olumetric and **I**so-contour based **M**orphological **A**symmetry) Score and visualization scheme, for the quantitative and qualitative assessment of breasts. The assessments are performed with the help of the breast boundaries and the location of the Sternal Notch on the
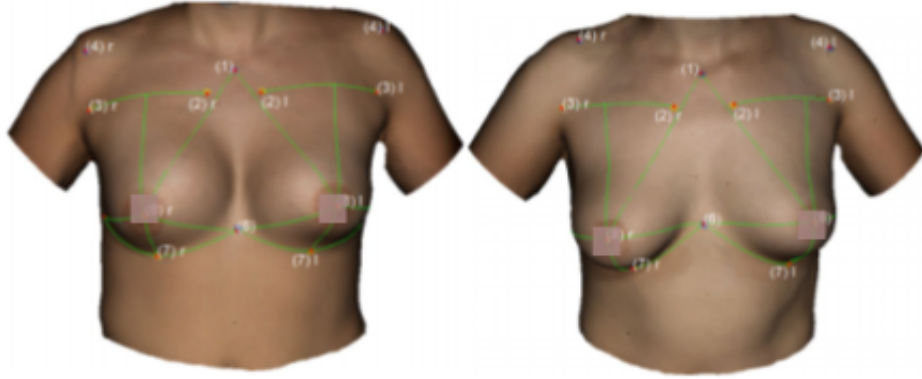
Figure 4.5: Illustration of state-of-the art digital anthropometry for breasts [66].
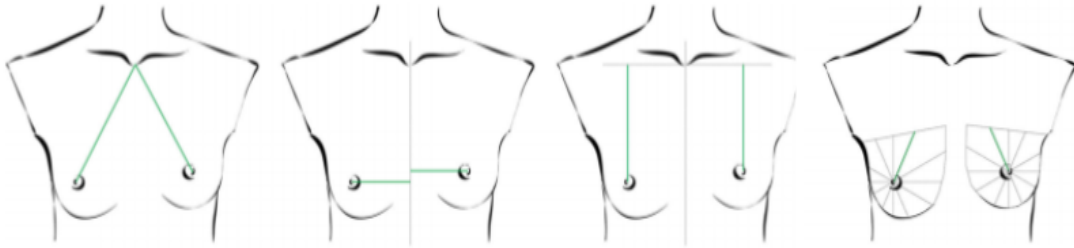
Figure 4.6: Illustration of breast analyzing tool (BAT) for symmetry analysis [67].

3D surface of the female torso.

4.3.1 Iso-countours

Similar to a topographical map seen in 2.2.1, we use marching squares algorithm [72], to compute the iso-contours [73] form the point cloud data, by using contour lines, (5) to describe the topography of the breast mounds, as showcased in Fig. 4.7.

Contour lines from breast surface $S(X, Y, Z) \in \mathbb{R}^3$ are:

$$\{(X, Y) \mid C(X, Y) = Z\}, \quad Z \in [0, z_{max}] \tag{5}$$

As 2D planar sections of the 3D breast surface, the iso-contours are parallel to the XY-plane. The contour lines from each iso-value (Z varying from lowest to the highest elevation, i.e., 0 to z_{max}) are used to generate binary masks by filling the areas inside the iso-contours as seen in

POINT CLOUD DATA **ISO-CONTOURS**
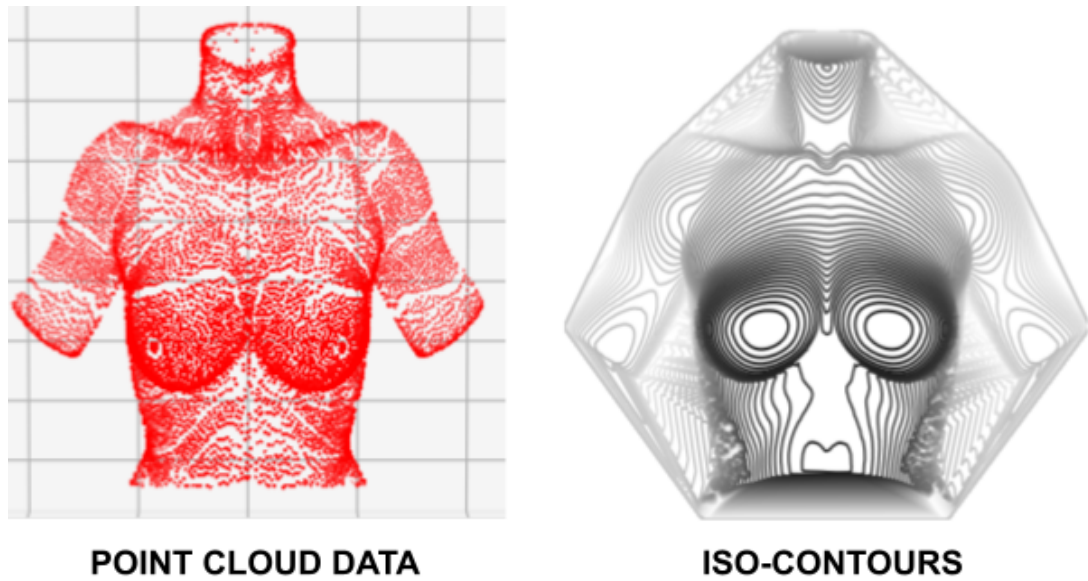
Figure 4.7: Iso-contours generated from input point cloud data.

ISO-CONTOURS **BINARY MASK FROM DIFFERENT ISO-VALUES(LEVELS)**
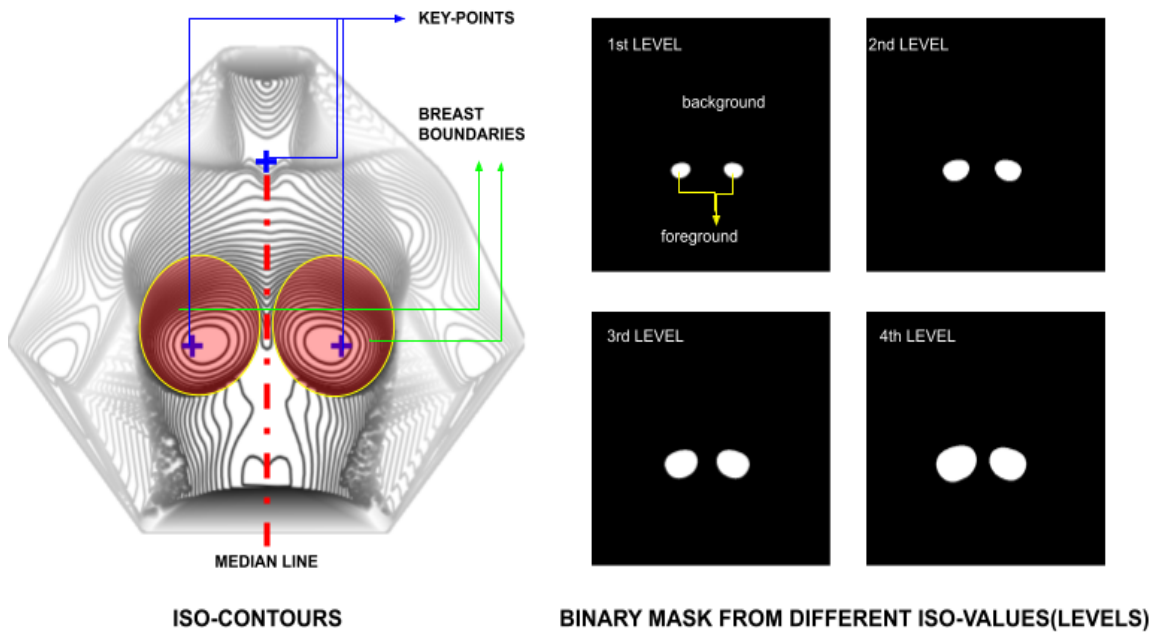
Figure 4.8: Illustration for generating binary masks from iso-contours at different iso-values or levels.

Fig. 4.8. In this work, we choose the right breast mound (image left) as the reference and the left breast mound (image right) as the target, as seen in Fig. 4.9. But in practice, the reference and target will be defined by the patient and observer based on personal preference.
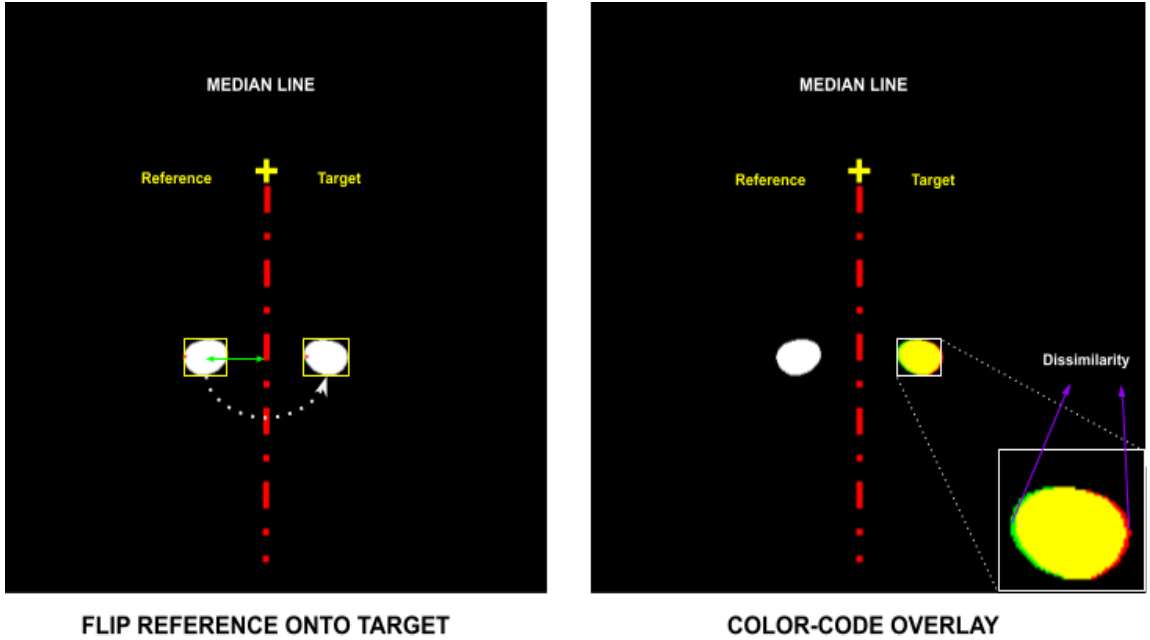
Figure 4.9: Functional Illustration of flipping the reference breast, along the median line [-90 deg line from key-point], onto the target breast and color coding of the overlay: **black** - is the image background or TN; **yellow** - regions present in both reference and target [similarity] or TP; **green** - region present in reference but absent in target [dissimilarity] or FN; **red** - region absent in the reference but present in the target [dissimilarity] or FP.

Then, at every iso-value Z we split the iso-contour into reference (right breast) and target (left breast), and flip the reference contour $R(X, Y)$ onto the target $T(X, Y)$ along the median line, given by (6), and color code the results to visualize the dissimilarity, as shown in Fig. 4.9, and repeat the process for all iso-values,

$$\{(X, Y) \mid \{R(X, Y), T(X, Y)\} \in C(X, Y) = Z \}, Z \in [0, z_{max}]$$

$$\{R^{'}(X, Y) = R(-X + 2D, Y)\} \qquad (6)$$

where $R^{'}$ is the flipped reference contour; and D is the x-intercept of the median line, $y = \frac{3\pi}{2} m_x + c$; and (m_x, m_y) are the coordinates of the sternal notch.

4.3.2 Breast Volume

To compute the individual volumes of the reference and target breast mounds V_1 and V_2, respectively, we add their surface areas form each iso-value, and find the overall volume difference

35

VISUALIZATION OF DISSIMILARITY AFTER RESTACKING
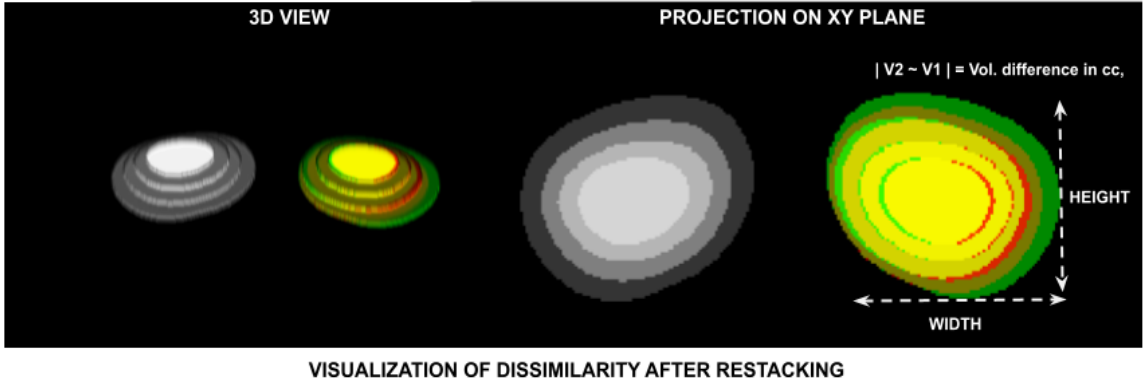
Figure 4.10: Illustration for visualization of qualitative information, detailing: volume difference, in cubic centimeters, between the reference and target breast mounds; base-width and base-height of the respective breast mounds; and color coded visualization of dissimilarity between both breast mounds. Here, the green and red regions indicate tissue mass that needs to be added or removed, respectively, to the target breast mound for reducing the overall asymmetry.

V_{DIFF} and volume ratio V_r as shown in (7),
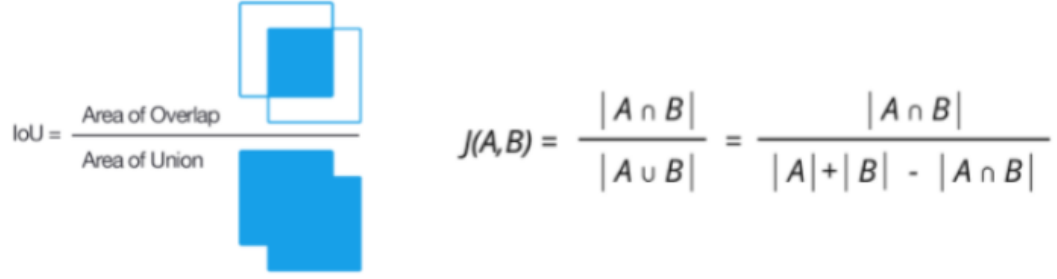
$$V_1 = \sum_{i=0}^{z_{max}} area\{R(X,Y) = i\} \quad V_2 = \sum_{i=0}^{z_{max}} area\{T(X,Y) = i\}$$

(7)

$$V_{DIFF} = |V_1 - V_2| \qquad V_r = \frac{min(V_1, V_2)}{max(V_1, V_2)}$$

4.3.3 Asymmetry Score

Unlike existing works from recent literature that rely on simple linear measurements, the proposed methodology, VIMA, utilizes the entire 3D morphology and the individual volumes of both the breast mounds. In Fig. 4.10, we illustrate the overlapping of the iso-contours from the reference onto the target for visualizing the dissimilarity through color coding. Measuring dissimilarity between between two 2D surfaces is similar to measuring quality of segmentation map with respect to the ground truth, hence, we use the Jaccard Index [48], commonly known as Intersection-over-Union (IoU) for assessment.

Instead of computing the IoU at every iso-value, and then averaging the results for producing a single measure of dissimilarity, we can compute the overall TP, TN, FP, FN across all iso-values; and find the overall dissimilarity between two breast mounds from (8), which is then used to compute the $VIMA$ score using a convex combination of $IOU_{overall}$ and volume V_r with λ empirically

36

Figure 4.11: Intersection over Union

set to 0.75 as seen in (9).

For $R'(X,Y)$ overlaid onto $T(X,Y)$:

		$T(X,Y) = i$	
		0	1
$R'(X,Y) = i$	0	$tn_i(0,0)$	$fp_i(0,1)$
	1	$fn_i(1,0)$	$tp_i(1,1)$

$$TP,\ TN,\ FP,\ FN\ =\ \sum_{i=0}^{z_{max}} tp_i,\ tn_i,\ fp_i,\ fn_i$$

$$IOU_{overall} = \frac{TP}{TP + FP + FN} \tag{8}$$

Using V_r from (7) and $IOU_{overall}$ from (8) we compute the VIMA score:

$$VIMA\ =\ 1\ -\ [\ \lambda(IOU_{overall})\ +\ (1-\lambda)V_r\ ],\ \text{where } \lambda = 0.75 \tag{9}$$

4.4 Experimental Setup

The proposed methodology was applied to point cloud data obtained from 3D scans of artificial breasts. The point clouds were acquired by employing the Scandy Pro application [74] on an iPhone 11 with an integrated time-of-flight sensor. The data was then exported to MeshLab for data

Figure 4.12: Illustration for first experiment (EXP1): **black** - (TN) is the background; **yellow** - (TP) regions present in both reference and target; **green** - (FN) need to add tissue volume of 82.32 cc; **red** - (FP) need to remove tissue volume of 37.51 cc;

inspection, sternal notch selection, and delineation of breast boundaries and stored as .pcl files. Two experiments were designed to evaluate the proposed method. For the first experiment (EXP1), 3D scans of breast mounds with volumes 260 ccs and 215 ccs were used as the reference and target, respectively. For the second experiment (EXP2) scans of two breasts of equal volume (215ccs) with different orientations with respect to the median line, were used.

The iso-contour visualizations were showcased to plastic surgeons for validation. Due to the restrictions caused by the COVID-19 pandemic, and the scheduling issues with doctors, our study sample only comprises three surgeons (from the US and Canada) that specialized in plastic and reconstructive surgeries. As part of the validation, their feedback on the method of assessment for quantifying breast asymmetry was documented based on a custom questionnaire inspired by the Likert Scale [75]. It is similar to the standardized psychometric scale method and consists of questions, each having a five-point scale value (1 to 5), with 1 and 5 corresponding to Strongly disagree and Strongly agree, respectively. Questions 1,3,5 each contribute towards the sum, with its : *scale value*; and questions 2,4,6 each contribute a quantity of *5 - scale value* to the sum. The result is then divided by the total sum (30) to produce the final utility score (U_{Score}).
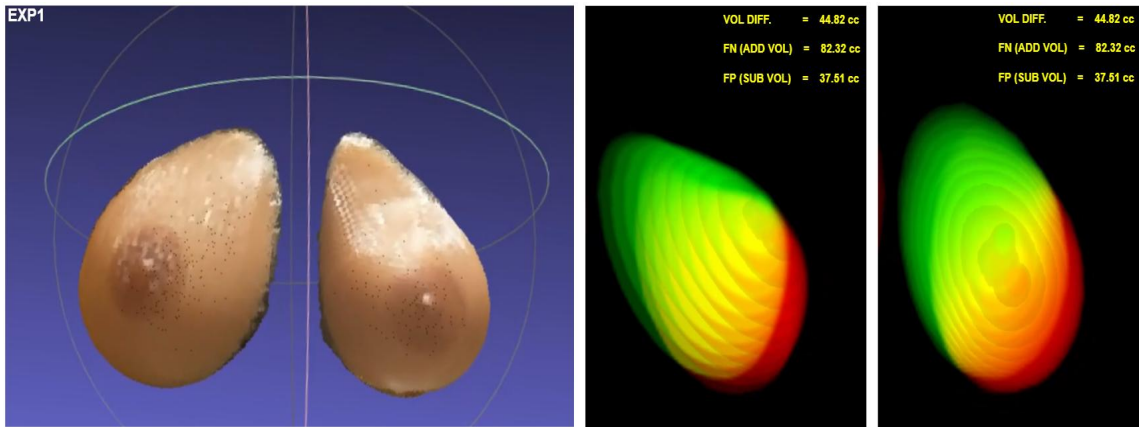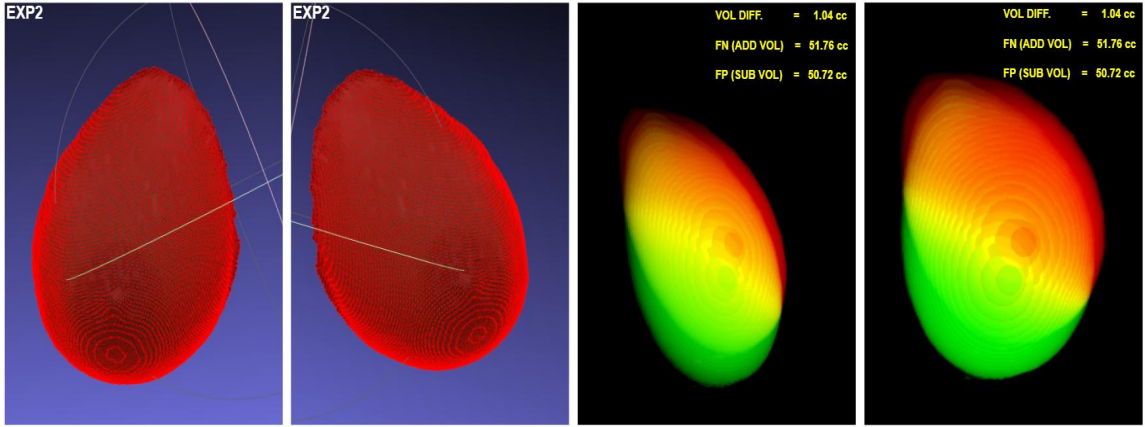
Figure 4.13: Illustration for second experiment (EXP2): **black** - (TN) is the background; **yellow** - (TP) regions present in both reference and target; **green** - (FN) need to add tissue volume of 51.76 cc; **red** - (FP) need to remove tissue volume of 50.72 cc;

Table 4.1: VIMA Experimentation.

EXPERIMENT	Reference (vol in cc)	Target(cc)	V_{DIFF} (cc)	$IOU_{overall}$ (%)	V_r(%)	VIMA(%)
EXP1	259.77	214.95	44.82	59.69	82.76	34.13
EXP2	214.95	213.91	1.04	62.62	99.41	28.18

4.5 Results

The quantitative results obtained from applying the VIMA methodology (5)-(9) to both experiments EXP1 and EXP2 are tabulated in Table 4.1. The results from the last column quantify the amount of dissimilarity between the two breasts in each experiment. The visualizations from VIMA on experiments EXP1 and EXP2 are respectively showcased in Figs. 4.12 and 4.13. It highlights the advantage of VIMA over conventional techniques by specifying – (a) regions that contribute to breast asymmetry; (b) quality or nature of dissimilarity i.e., dissimilarity due to lack or excess of breast tissue at the specific region; and (c) the amount or quantity of breast tissue at the target region. The overall utility based on surgeon's feedback is tabulated in Table 4.2, where VIMA was found to be *highly useful* and easy to follow.

4.6 Discussion

On analysing the data in Table 4.1, the proposed methodology showcases that the breasts from EXP2 are more symmetrical due to a lower VIMA score, as opposed to the breasts from EXP1.

Table 4.2: Likert assessment for VIMA visualization.

VIMA Utility Questions \ Subjects	S1	S2	S3
I think I would use it frequently	5	4	5
I think it is hard to follow	1	2	1
I think it is well integrated as a methodology	4	3	4
I would not require technical support to use it	2	1	2
It is better than linear measures	5	5	4
It is hard to track changes peri-operatively	1	2	1
SUM	25	22	24
$U_{Score}(\%)$	83.34	73.34	80

The minor variations in the volume measures can be attributed to the interpolation operation in the marching squares algorithm, used in the generation of iso-contours. The visualizations from Figs. 4.12 and 4.13 highlight the efficacy of VIMA, especially in EXP2 by showcasing that even with breasts of the same volume, a person can have asymmetry due to change in the overall shape. This is further complemented by VIMA's ability to locate, delineate and measure breast regions that contribute towards asymmetry, and provide an absolute measure through the VIMA Score. Based on assessments from Table 4.2, we can deduce that the methodology was found by surgeons to be very easy to follow and of high utility for decision making during surgery. While the Likert assessment serves as a validation (informal) for the proposed methodology, a clinical trial is necessary to establish VIMA as a new baseline within the research community.

4.7 Conclusions

In this chapter, we showcased a new methodology using Radiomics called VIMA (**V**olumetric and **I**so-contour based **M**orphological **A**symmetry) for performing the quantitative assessment of breast morphology, for aiding plastic surgeons in reducing the incidence of breast asymmetry from aesthetic breast surgeries. Unlike existing works from recent literature, that rely on linear measurements for describing the breast morphology to compute breast asymmetry, the proposed methodology takes into account the entire shape and volume of the individual breast mounds and highlights the exact regions that contribute to asymmetry. VIMA was found by surgeons to be very easy to understand and highly useful for making decisions during breast surgeries.

Chapter 5

Conclusions and Future work

This chapter we summarize our work and provide some future directions for this thesis.

5.1 Conclusions

In this thesis, we explored Radiomics in medical imaging by applying the best scientific data to the relevant clinical expertise, for improving utility and decision-making in a clinical setting. We focused on two applications: pelvic bone segmentation from CT data for designing patient-specific customizable pessaries; and quantitative assessment of breast morphology, for breast surgeries.

For pelvic bone segmentation, we investigated several encoder-decoder network configurations trained on limited data and use histogram based features from Radiomics to take a data-centric view towards the problem and boost the model performance on completely unseen data through histogram specification. Then we evaluated the performance on two publicly available CT datasets.

For the assessment of breast morphology, we proposed a novel metric for quantifying the overall dissimilarity between two breast mounds, called VIMA, by using shape and size based features from iso-contours. The methodology was experimented on 3D scans of artificial breasts and found to be highly useful in an intra-operative setting for aiding surgeons in sculpting patients' breasts during aesthetic and reconstructive breast surgeries.

5.2   Future Work

Some possible directions for future works in pelvic-bone segmentation are:

Deep learning based Image Enhancement

In our segmentation work, a 1×256 feature vector representing the image tonal distribution (histogram) was used for morphing the unseen data. Hence, deep learning based single image contrast enhancement (SICE) technique [76] can be employed for producing better morphing of tonal values. This could lead to even higher segmentation performance for networks trained on limited data.

Attention Mechanisms

Similar to a focusing mechanism in human vision, attention mechanisms [77, 78] in deep learning can be utilized in the segmentation pipeline. These methods suppress the information from the unimportant regions of an image and inform the network on where to focus. This aids the network in capturing rich features, which can further improve the segmentation performance.

Better loss function

In our segmentation work we utilized a weighted sum of BCE and IOU loss function. Since, most loss functions focus on pixel level classification error, structural priors like [79] could be incorporated to better train the model for achieving high correlation between ground truth and predictions.

Possible direction for future work in assessment of breast dissimilarity is:

Automated localization and segmentation using Gaussian Curvature

Techniques like Mean and Gaussian curvature filtering [80] can be employed for the automated detection and localization of sternal notch and nipple-areolar complex. Furthermore, projections of the curvature response can be utilized for segmenting breast boundaries in an automated fashion.

Bibliography

[1] A. M. Reitsma and J. D. Moreno, "Ethics of innovative surgery: Us surgeons' definitions, knowledge, and attitudes," *Journal of the American College of Surgeons*, vol. 200, no. 1, pp. 103–110, 2005.

[2] S. Timmermans and E. S. Kolker, "Evidence-based medicine and the reconfiguration of medical knowledge," *Journal of health and social behavior*, pp. 177–193, 2004.

[3] D. L. Sackett, W. M. Rosenberg, J. M. Gray, R. B. Haynes, and W. S. Richardson, "Evidence based medicine: what it is and what it isn't," pp. 71–72, 1996.

[4] J. E. van Timmeren, D. Cester, S. Tanadini-Lang, H. Alkadhi, and B. Baessler, "Radiomics in medical imaging—"how-to" guide and critical reflection," *Insights into imaging*, vol. 11, no. 1, pp. 1–16, 2020.

[5] S. H. Song, H. Park, G. Lee, H. Y. Lee, I. Sohn, H. S. Kim, S. H. Lee, J. Y. Jeong, J. Kim, K. S. Lee *et al.*, "Imaging phenotyping using radiomics to predict micropapillary pattern within lung adenocarcinoma," *Journal of Thoracic Oncology*, vol. 12, no. 4, pp. 624–632, 2017.

[6] G. D. Tourassi, "Journey toward computer-aided diagnosis: role of image texture analysis," *Radiology*, vol. 213, no. 2, pp. 317–320, 1999.

[7] Z. Liu, S. Wang, J. W. Di Dong, C. Fang, X. Zhou, K. Sun, L. Li, B. Li, M. Wang, and J. Tian, "The applications of radiomics in precision diagnosis and treatment of oncology: opportunities and challenges," *Theranostics*, vol. 9, no. 5, p. 1303, 2019.

[8] I. Bankman, *Handbook of medical image processing and analysis*. Elsevier, 2008.

[9] S. M. Anwar, M. Majid, A. Qayyum, M. Awais, M. Alnowami, and M. K. Khan, "Medical image analysis using convolutional neural networks: a review," *Journal of medical systems*, vol. 42, no. 11, pp. 1–13, 2018.

[10] E. Nasr-Esfahani, S. Samavi, N. Karimi, S. R. Soroushmehr, K. Ward, M. H. Jafari, B. Felfeliyan, B. Nallamothu, and K. Najarian, "Vessel extraction in x-ray angiograms using deep learning," in *2016 38th Annual international conference of the IEEE engineering in medicine and biology society (EMBC)*. IEEE, 2016, pp. 643–646.

[11] E. Bye and E. McKinney, "Fit analysis using live and 3d scan models," *International Journal of Clothing Science and Technology*, 2010.

[12] G. J. Iddan and G. Yahav, "Three-dimensional imaging in the studio and elsewhere," in *Three-Dimensional Image Capture and Applications IV*, vol. 4298. International Society for Optics and Photonics, 2001, pp. 48–55.

[13] N. Sharma and L. M. Aggarwal, "Automated medical image segmentation techniques," *Journal of medical physics/Association of Medical Physicists of India*, vol. 35, no. 1, p. 3, 2010.

[14] E. L. Usery and T. Hahmann, "What is in a contour map? a region-based logical formalization of contour semantics," 2015.

[15] I. Mpiperis, S. Malasiotis, and M. G. Strintzis, "3d face recognition by point signatures and iso-contours," *Proc. of SPPRA*, 2007.

[16] S. P. Morse, "Concepts of use in contour map processing," *Communications of the ACM*, vol. 12, no. 3, pp. 147–152, 1969.

[17] "Marching squares," https://en.wikipedia.org/wiki/Marching_squares.

[18] K. He, X. Zhang, S. Ren, and J. Sun, "Deep residual learning for image recognition," in *Proceedings of the IEEE conference on computer vision and pattern recognition*, 2016, pp. 770–778.

[19] C. Szegedy, V. Vanhoucke, S. Ioffe, J. Shlens, and Z. Wojna, "Rethinking the inception architecture for computer vision," in *Proceedings of the IEEE conference on computer vision and pattern recognition*, 2016, pp. 2818–2826.

[20] O. Ronneberger, P. Fischer, and T. Brox, "U-net: Convolutional networks for biomedical image segmentation," in *International Conference on Medical image computing and computer-assisted intervention*.   Springer, 2015, pp. 234–241.

[21] J. Long, E. Shelhamer, and T. Darrell, "Fully convolutional networks for semantic segmentation," in *Proceedings of the IEEE conference on computer vision and pattern recognition*, 2015, pp. 3431–3440.

[22] A. Krizhevsky, I. Sutskever, and G. E. Hinton, "Imagenet classification with deep convolutional neural networks," *Advances in neural information processing systems*, vol. 25, 2012.

[23] "Medium: Cnns," https://medium.com/techiepedia/binary-image-classifier-cnn-using-tensorflow-a3f5d6746697.

[24] "Jermy jordan: Intro to cnns," https://www.jeremyjordan.me/convolutional-neural-networks/.

[25] F. Milletari, N. Navab, and S.-A. Ahmadi, "V-net: Fully convolutional neural networks for volumetric medical image segmentation," in *2016 fourth international conference on 3D vision (3DV)*.   IEEE, 2016, pp. 565–571.

[26] "Understanding and designing the female pelvic anatomy, a measuring device and an intravaginal device using 3-dimensional modeling techniques and artificial intelligence," https://www.mitacs.ca/en/projects/understanding-and-designing-female-pelvic-anatomy-measuring-device-and-intravaginal-device, 2020.

[27] CHEROKEE, "Women's Health Specialists," https://cherokeewomenshealth.com/2021/02/pelvic-organ-prolapse-at-just-32-years-old/.

[28] K. A. Jones, J. P. Shepherd, S. S. Oliphant, L. Wang, C. H. Bunker, and J. L. Lowder, "Trends in inpatient prolapse procedures in the united states, 1979–2006," *American journal of obstetrics and gynecology*, vol. 202, no. 5, pp. 501–e1, 2010.

[29] W. Post, "Vaginal mesh has caused health problems," https://www.washingtonpost.com/national/health-science/vaginal-mesh-has-caused-health-problems-in-many-women-even-as-some-surgeons-vouch-for-its-safety-and-efficacy/2019/01/18/1c4a2332-ff0f-11e8-ad40-cdfd0e0dd65a_story.html/.

[30] mayoclinic, "Pessary types," https://www.mayoclinic.org/diseases-conditions/urinary-incontinence/multimedia/pessary-use/img-20006056.

[31] H. Yu, H. Wang, Y. Shi, K. Xu, X. Yu, and Y. Cao, "The segmentation of bones in pelvic CT images based on extraction of key frames," *BMC medical imaging*, vol. 18, no. 1, p. 18, 2018.

[32] P. T. Truc, S. Lee, and T.-S. Kim, "A density distance augmented chan-vese active contour for CT bone segmentation," in *2008 30th Annual International Conference of the IEEE Engineering in Medicine and Biology Society*. IEEE, 2008, pp. 482–485.

[33] D. Kainmueller, H. Lamecker, S. Zachow, and H.-C. Hege, "Coupling deformable models for multi-object segmentation," in *International Symposium on Biomedical Simulation*. Springer, 2008, pp. 69–78.

[34] H. Wang, J. W. Suh, S. R. Das, J. B. Pluta, C. Craige, and P. A. Yushkevich, "Multi-atlas segmentation with joint label fusion," *IEEE transactions on pattern analysis and machine intelligence*, vol. 35, no. 3, pp. 611–623, 2012.

[35] H. Wang, M. Moradi, Y. Gur, P. Prasanna, and T. Syeda-Mahmood, "A multi-atlas approach to region of interest detection for medical image classification," in *International Conference on Medical Image Computing and Computer-Assisted Intervention*. Springer, 2017, pp. 168–176.

[36] F. Yokota, T. Okada, M. Takao, N. Sugano, Y. Tada, N. Tomiyama, and Y. Sato, "Automated CT segmentation of diseased hip using hierarchical and conditional statistical shape models," in *International Conference on Medical Image Computing and Computer-Assisted Intervention*. Springer, 2013, pp. 190–197.

46

[37] C. Chu, J. Bai, X. Wu, and G. Zheng, "MASCG: Multi-Atlas Segmentation Constrained Graph method for accurate segmentation of hip CT images," *Medical image analysis*, vol. 26, no. 1, pp. 173–184, 2015.

[38] G. Zeng, X. Yang, J. Li, L. Yu, P.-A. Heng, and G. Zheng, "3D U-net with multi-level deep supervision: fully automatic segmentation of proximal femur in 3D MR images," in *International workshop on machine learning in medical imaging*. Springer, 2017, pp. 274–282.

[39] F. Chen, J. Liu, Z. Zhao, M. Zhu, and H. Liao, "Three-dimensional feature-enhanced network for automatic femur segmentation," *IEEE journal of biomedical and health informatics*, vol. 23, no. 1, pp. 243–252, 2017.

[40] Y. Chang, Y. Yuan, C. Guo, Y. Wang, Y. Cheng, and S. Tamura, "Accurate pelvis and femur segmentation in hip CT with a novel patch-based refinement," *IEEE journal of biomedical and health informatics*, vol. 23, no. 3, pp. 1192–1204, 2018.

[41] P. Liu, H. Han, Y. Du, H. Zhu, Y. Li, F. Gu, H. Xiao, J. Li, C. Zhao, L. Xiao *et al.*, "Deep learning to segment pelvic bones: large-scale ct datasets and baseline models," *International Journal of Computer Assisted Radiology and Surgery*, vol. 16, no. 5, pp. 749–756, 2021.

[42] M. Tan and Q. V. Le, "Efficientnet: Rethinking model scaling for convolutional neural networks," *arXiv preprint arXiv:1905.11946*, 2019.

[43] R. Szeliski, *Computer vision: algorithms and applications*. Springer Science & Business Media, 2010.

[44] J. Schindelin, I. Arganda-Carreras, E. Frise, V. Kaynig, M. Longair, T. Pietzsch, S. Preibisch, C. Rueden, S. Saalfeld, B. Schmid *et al.*, "Fiji: an open-source platform for biological-image analysis," *Nature methods*, vol. 9, no. 7, pp. 676–682, 2012.

[45] K. Clark, B. Vendt, K. Smith, J. Freymann, J. Kirby, P. Koppel, S. Moore, S. Phillips, D. Maffitt, M. Pringle *et al.*, "The cancer imaging archive TCIA: maintaining and operating a public information repository," *Journal of digital imaging*, vol. 26, no. 6, pp. 1045–1057, 2013.

[46] M. J. Ackerman, "The visible human project," *Proceedings of the IEEE*, vol. 86, no. 3, pp. 504–511, 1998.

[47] W. R. Crum, O. Camara, and D. L. Hill, "Generalized overlap measures for evaluation and validation in medical image analysis," *IEEE Trans. Med. Imag.*, vol. 25, no. 11, pp. 1451–1461, 2006.

[48] H.-H. Chang, A. H. Zhuang, D. J. Valentino, and W.-C. Chu, "Performance measure characterization for evaluating neuroimage segmentation algorithms," *Neuroimage*, vol. 47, no. 1, pp. 122–135, 2009.

[49] P. Yakubovskiy, "Segmentation models," https://segmentation-models.readthedocs.io/en/latest/, 2019.

[50] J. Deng, W. Dong, R. Socher, L.-J. Li, K. Li, and L. Fei-Fei, "Imagenet: A large-scale hierarchical image database," in *2009 IEEE conference on computer vision and pattern recognition*. Ieee, 2009, pp. 248–255.

[51] P. Jois, "Qualitative assessment of breast asymmetry using 3-dimensional modeling, with computer vision and deep learning," https://www.mitacs.ca/en/projects/qualitative-assessment-breast-asymmetry-using-3-dimensional-modeling-computer-vision-and, 2021.

[52] J. Semple, K. A. Metcalfe, H. T. Lynch, C. Kim-Sing, L. Senter, T. Pal, P. Ainsworth, J. Lubinski, N. Tung, C. Eng *et al.*, "International rates of breast reconstruction after prophylactic mastectomy in brca1 and brca2 mutation carriers," *Annals of surgical oncology*, vol. 20, no. 12, pp. 3817–3822, 2013.

[53] K. E. Türk and M. Yılmaz, "The effect on quality of life and body image of mastectomy among breast cancer survivors," *European journal of breast health*, vol. 14, no. 4, p. 205, 2018.

[54] J. Bostwick, *Plastic and reconstructive breast surgery*. Quality Medical Pub., 1990, vol. 2.

[55] K. Sneeuw, N. Aaronson, J. Yarnold, M. Broderick, J. Regan, G. Ross, and A. Goddard, "Cosmetic and functional outcomes of breast conserving treatment for early stage breast cancer. 1.

comparison of patients' ratings, observers' ratings and objective assessments," *Radiotherapy and oncology*, vol. 25, no. 3, pp. 153–159, 1992.

[56] T. L. H. Brown, C. Ringrose, R. Hyland, A. Cole, and T. Brotherston, "A method of assessing female breast morphometry and its clinical application," vol. 52, no. 5.   Elsevier, 1999, pp. 355–359.

[57] W.H.O., "Breast Cancer Early Diagnosis and Screening," https://www.who.int/news-room/fact-sheets/detail/breast-cancer, 2019.

[58] L. Yuen-Jong, *Aesthetics of the female breast: correlation of pluralistic evaluations with volume and surface area*.   Yale Digital Library, 2009.

[59] WikiHow, "Breast volume test," https://www.wikihow.com/Weigh-Your-Breasts#/Image:Weigh-Your-Breasts/.

[60] J. C. Lowery, E. G. Wilkins, W. M. Kuzon, and J. A. Davis, "Evaluations of aesthetic results in breast reconstruction: an analysis of reliability." *Annals of plastic surgery*, vol. 36, no. 6, pp. 601–6, 1996.

[61] R. D. Pezner, J. A. Lipsett, N. L. Vora, and K. R. Desai, "Limited usefulness of observer-based cosmesis scales employed to evaluate patients treated conservatively for breast cancer," *International Journal of Radiation Oncology* Biology* Physics*, vol. 11, no. 6, pp. 1117–1119, 1985.

[62] J. Lee, M. Kawale, F. A. Merchant, J. Weston, M. C. Fingeret, D. Ladewig, G. P. Reece, M. A. Crosby, E. K. Beahm, and M. K. Markey, "Validation of stereophotogrammetry of the human torso," *Breast cancer: basic and clinical research*, vol. 5, pp. BCBCR–S6352, 2011.

[63] A. Losken, H. Seify, D. D. Denson, A. A. Paredes Jr, and G. W. Carlson, "Validating three-dimensional imaging of the breast," *Annals of plastic surgery*, vol. 54, no. 5, pp. 471–476, 2005.

[64] D. Sheffer, R. Herron, W. Morek, F. Proietti-Orlandi, C. Loughry, R. Hamor, R. Liebelt, and

R. Varga, "Stereophotogrammetric method for breast cancer detection," in *Biostereometrics' 82*, vol. 361. SPIE, 1983, pp. 120–124.

[65] W. Krois, A. K. Romar, T. Wild, P. Dubsky, R. Exner, P. Panhofer, R. Jakesz, M. Gnant, and F. Fitzal, "Objective breast symmetry analysis with the breast analyzing tool (bat): improved tool for clinical trials," *Breast cancer research and treatment*, vol. 164, no. 2, pp. 421–427, 2017.

[66] R. Hartmann, M. Weiherer, D. Schiltz, M. Baringer, V. Noisser, V. Hösl, A. Eigenberger, S. Seitz, C. Palm, L. Prantl *et al.*, "New aspects in digital breast assessment: further refinement of a method for automated digital anthropometry," *Archives of gynecology and obstetrics*, vol. 303, no. 3, pp. 721–728, 2021.

[67] M. Eder, F. v. Waldenfels, A. Swobodnik, M. Klöppel, A.-K. Pape, T. Schuster, S. Raith, E. Kitzler, N. A. Papadopulos, H.-G. Machens *et al.*, "Objective breast symmetry evaluation using 3-d surface imaging," *The Breast*, vol. 21, no. 2, pp. 152–158, 2012.

[68] K. Minolta, "Vivid 3d digitizer," https://www.upc.edu/sct/ca/documents_equipament/d_288_id-715.pdf, 2002.

[69] C. Scientific, "Vectra XT 3D Imaging Systems," https://www.canfieldsci.com/imaging-systems/vectra-xt-3d-imaging-system/, 2022.

[70] Y. Yang, D. Mu, B. Xu, W. Li, X. Zhang, Y. Lin, and H. Li, "An intraoperative measurement method of breast symmetry using three-dimensional scanning technique in reduction mammaplasty," *Aesthetic Plastic Surgery*, vol. 45, no. 5, pp. 2135–2145, 2021.

[71] S. Amini and M. Kersten-Oertel, "Augmented reality mastectomy surgical planning prototype using the hololens template for healthcare technology letters," *Healthcare Technology Letters*, vol. 6, no. 6, p. 261, 2019.

[72] C. Maple, "Geometric design and space planning using the marching squares and marching cube algorithms," in *2003 international conference on geometric modeling and graphics, 2003. Proceedings*. IEEE, 2003, pp. 90–95.

[73] H. R. R. Courant, R. Courant, H. Robbins, I. Stewart *et al.*, *What is Mathematics?: an elementary approach to ideas and methods*. Oxford University Press, USA, 1996.

[74] "Scandy pro: 3d scanning," https://www.scandy.co/.

[75] "Likert scale," https://en.wikipedia.org/wiki/Likert_scale.

[76] J. Cai, S. Gu, and L. Zhang, "Learning a deep single image contrast enhancer from multi-exposure images," *IEEE Transactions on Image Processing*, vol. 27, no. 4, pp. 2049–2062, 2018.

[77] J. Fu, J. Liu, H. Tian, Y. Li, Y. Bao, Z. Fang, and H. Lu, "Dual attention network for scene segmentation," in *Proceedings of the IEEE/CVF conference on computer vision and pattern recognition*, 2019, pp. 3146–3154.

[78] Z. Huang, X. Wang, L. Huang, C. Huang, Y. Wei, and W. Liu, "Ccnet: Criss-cross attention for semantic segmentation," in *Proceedings of the IEEE/CVF International Conference on Computer Vision*, 2019, pp. 603–612.

[79] S. Zhao, B. Wu, W. Chu, Y. Hu, and D. Cai, "Correlation maximized structural similarity loss for semantic segmentation," *arXiv preprint arXiv:1910.08711*, 2019.

[80] M. M. Kawale, G. P. Reece, M. A. Crosby, E. K. Beahm, M. C. Fingeret, M. K. Markey, and F. A. Merchant, "Automated identification of fiducial points on 3d torso images," *Biomedical Engineering and Computational Biology*, vol. 5, pp. BECB–S11 800, 2013.